

MICROCOPY RESOLUTION TEST CHART  
NATIONAL BUREAU OF STANDARDS 1963-A

12



AD-A149 799

Department of Aeronautics  
Dean of the Faculty  
United States Air Force Academy  
Colorado Springs  
Colorado 80840-5831

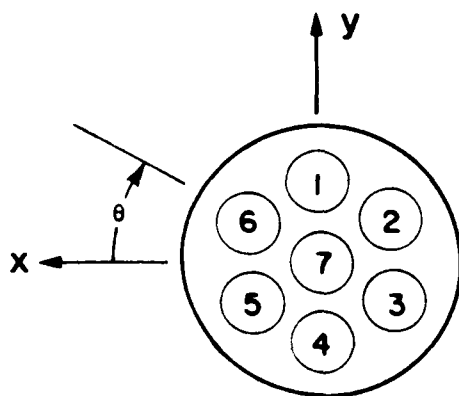
THE SEVEN-HOLE PRESSURE PROBE

TECHNICAL NOTE  
USAFA-TN-84-9

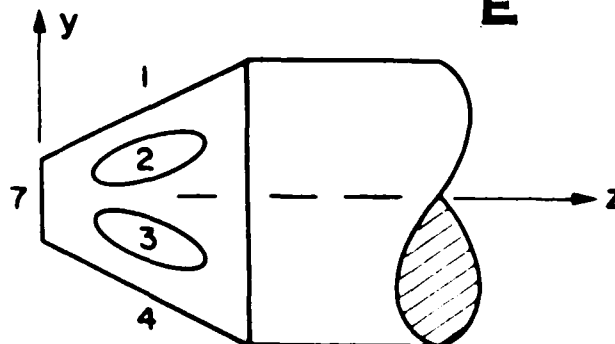
Reed, L.  
Mattingly, J.D.  
Jonas, F.M.

DTIC  
ELECTE  
S D  
JAN 25 1985  
E

DTIC FILE COPY



FRONT VIEW



SIDE VIEW

Any views expressed in this paper are those of the authors. They should not be interpreted as reflecting the views of the USAF Academy or the official opinion of any governmental agency. Notes are not reviewed for content or quality by the USAF Academy but are published primarily as a service to the faculty to facilitate internal research communication.

This Technical Note has been cleared for open publication and/or public release by the appropriate Office of Information in accordance with AFR 190\*1 and DODD 5230.9. There is no objection to unlimited distribution of this Technical Note to the public at large or by DDC to the National Technical Information Service.

This Technical Note is approved for publication.



THOMAS E. McCANN, Lt Colonel, USAF  
Director of Research and Computer Based Education



# THE SEVEN-HOLE PRESSURE PROBE

Lawrence Reed\*, Jack D. Mattingly\*\*, and Frederick Jonas\*\*

## Abstract

This paper documents recent and past developments with respect to the seven-hole pressure probe. Included are discussions on probe design, construction, calibration, and measurement capabilities. The effects on probe measurements in shear flows, as well as methods of correction, are also included. Finally, research applications in the measurement of unknown flowfields are presented. As shown, the seven-hole pressure probe is a valuable and highly accurate device for qualitatively or quantitatively documenting unknown flowfields.

## 1. Introduction

The purpose of this paper is to document recent and past developments with respect to the seven-hole pressure probe developed at the United States Air Force Academy in conjunction with the NASA Ames Research Center. As with all pressure probes, the seven-hole probe can be used to map unknown internal or external flowfields, giving valuable information to the aerodynamicist. The advantage of the seven-hole probe over other flowfield measuring devices is its widely expanded measurement range and flexibility. To document this effort, Section II presents brief background material about the probe's design and use. Section III includes an overview of probe calibration in uniform flows, both compressible and incompressible. In Section IV, recent results of investigations into probe measurement capabilities in shear flow environments are presented. Measurement capabilities as well as measurement sources of error

---

\*and Lt., USAF, Graduate Student, Univ. of Washington

\*\*Major, USAF, Associate Professor, Dept. of Aeronautics



was developed at the United States Air Force Academy to increase the measurement range of a non-nulling pressure probe while minimizing probe size.

#### A. Nulling Versus Stationary Probes

The increased measurement range of a multi-hole probe revolves on its ability to sense more pressures at the face of the probe. Two procedures, nulling and stationary, may be used to acquire the pressure data. A nulling probe is rotated in one or two planes until opposing peripheral ports measure equal pressures. The corresponding angle of rotation determines the flow angle. For the non-nulling approach, the probe is held stationary as pressures in opposing peripheral ports are recorded. The pressure differences are then transformed to flow angles through previously known calibration relationships. Although the nulling procedure allows analysis of high angle flow, it is mechanically complex, time consuming, and hence, may not be cost effective. On the other hand, stationary probes with up to five holes are incapable of accurate measurements at high local flow angles (greater than 30 degrees) because of flow separation around the probe tip. Explained in detail in a later section, the seven hole probe is the only non-nulling probe that can determine flow angles up to 70 degrees relative to its axis. When combined with a computerized data acquisition system, the probe may record nearly two data points per second. This rate is significantly faster than current nulling devices, which require considerable time for the balancing of probe tip pressures before each measurement can be taken (Ref. 2).

#### B. Analytical Model of Pressure Probe



While numerically solving the three-dimensional potential flow equations for the flow around an aerodynamic probe may be more accurate than slender body theory under some conditions (Ref. 21 and 22), it does not lend itself to synthesis of probe shapes. The slender body approach to the analysis of the probe provides a basis for formulating analytic calibration relations and considerable insight into the physical process.

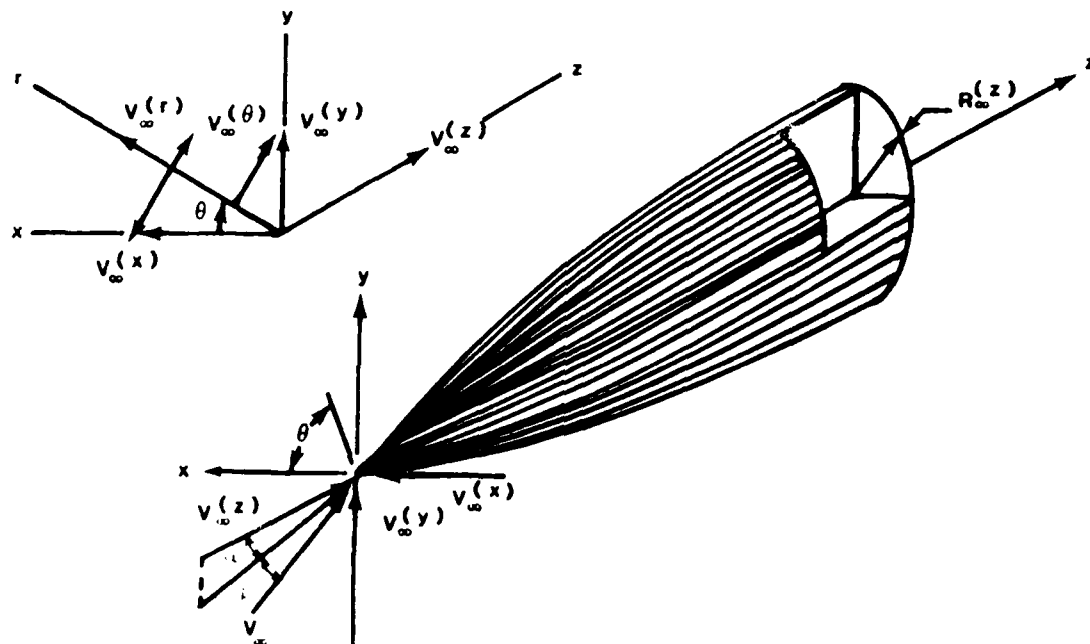


**Figure 2. SLENDER BODY OF REVOLUTION IN A CROSS-FLOW (REF.18)**

Huffman modeled the probe as a yawed body of revolution as shown in Figure 2. For a slender body, the equation of motion is linear and Huffman wrote the velocity potential as the sum of the axial flow and the cross flow components (this follows a method specified by Liepmann and Roshko, Ref. 23). Solution of the equation of motion yielded the following velocity field in cylindrical coordinates:

$$\begin{aligned} \frac{v_r}{V_\infty} &= R' \frac{R}{r} (\cos\alpha \cos\beta) + \left(1 - \frac{R^2}{r^2}\right) (\sin\beta \cos\theta + \sin\alpha \cos\beta \sin\theta) \\ \frac{v_\theta}{V_\infty} &= \left(1 + \frac{R^2}{r^2}\right) (\sin\alpha \cos\beta \cos\theta - \sin\beta \sin\theta) \\ \frac{v_z}{V_\infty} &= \left(1 + \frac{f}{2}\right) (\cos\alpha \cos\beta) + 2R' \frac{R}{r} (\sin\beta \cos\theta + \sin\alpha \cos\beta \sin\theta) \end{aligned} \quad (1)$$

where  $f$  denotes the body-geometry function given by

$$\begin{aligned} f &= -\frac{1}{2}(R')' \left( \frac{1}{\sqrt{z^2 + \delta^2 r^2}} - \frac{1}{\sqrt{(l-z)^2 + \delta^2 r^2}} \right) \\ &+ \frac{1}{2}(R')'' \left[ \frac{z-z}{\sqrt{(l-z)^2 + \delta^2 r^2}} + \frac{z}{\sqrt{z^2 + \delta^2 r^2}} + \psi n \left( \frac{-z + \sqrt{z^2 + \delta^2 r^2}}{\sqrt{(l-z)^2 + \delta^2 r^2}} \right) \right] \\ &- \frac{1}{4}(R')''' \left( \frac{z^2}{\sqrt{z^2 + \delta^2 r^2}} - \frac{(l-z)^2}{\sqrt{(l-z)^2 + \delta^2 r^2}} + 2 \sqrt{(l-z)^2 + \delta^2 r^2} - 2 \sqrt{z^2 + \delta^2 r^2} \right) + \dots \end{aligned} \quad (2)$$

The superscript prime (') denotes the derivative with respect to the variable  $z$ , and  $\delta^2 = 1 - M_\infty^2$ .

The pressure coefficient is defined as

$$C_p = \frac{P - P_\infty}{\frac{1}{2} \rho V_\infty^2} = 1 - \frac{V^2}{V_\infty^2} \quad (3)$$

And when evaluated on the body the following expression results:

$$C_p = 1 - \frac{v_r^2 + v_\theta^2 + v_z^2}{V_\infty^2} = 1 - \frac{R'^2 \cos^2\alpha \cos^2\beta + \sin^2\beta [1 - 4\sin^2\theta - 4(R')' \cos^2\theta]}{V_\infty^2} \quad (4)$$

where  $f$  is to be evaluated on the body surface, i.e.  $r=R$ , Equation 4 represents the major result of Huffman's analysis and can be used to determine probe angular and static pressure sensitivity for arbitrary geometries.

The pressure difference between ports on opposite sides of the probe is used to determine the flow angularity. Since the side ports of the probe are at the same  $z$  and  $r$  locations, the pressure difference is proportional to the difference of  $C_p$  values at different  $\theta$  locations and

$$\begin{aligned}
 p_i - p_j = & 4\sin^2\alpha [\sin^2\theta_j - \sin^2\theta_i + (R')^2 (\cos^2\theta_j - \cos^2\theta_i)] \\
 & + 4\sin^2\alpha \cos^2\beta [\cos^2\theta_j - \cos^2\theta_i + (R')^2 (\sin^2\theta_j - \sin^2\theta_i)] \quad (3) \\
 & + 2\sin\alpha \sin 2\beta [1 - (R')^2] [\sin 2\theta_i - \sin 2\theta_j] \\
 & - 2R'(1+f/2) [\cos\alpha \sin 2\beta (\cos\theta_i - \cos\theta_j) + \sin 2\alpha \cos^2\beta (\sin\theta_i - \sin\theta_j)]
 \end{aligned}$$

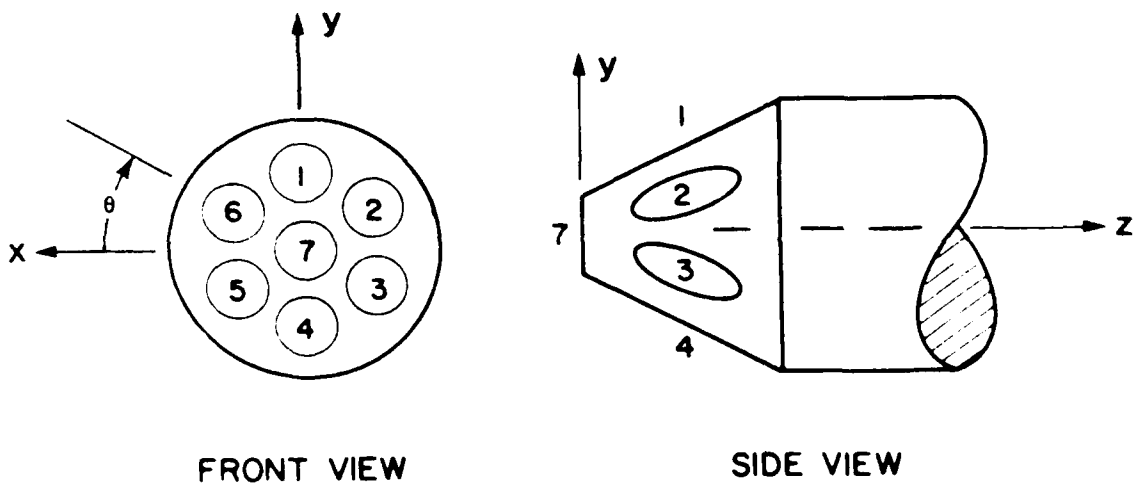


Figure 3. SEVEN-HOLE PROBE

For the seven-hole probe shown in Figure 3, the six holes on the side face are located at  $\theta_1=90^\circ$ ,  $\theta_2=150^\circ$ ,  $\theta_3=210^\circ$ ,  $\theta_4=270^\circ$ ,  $\theta_5=330^\circ$ , and  $\theta_6=30^\circ$ . The resulting three pressure coefficient differences for opposite side holes are

$$\begin{aligned} \Delta C_{14} &= C_{P_4} - C_{P_1} = 4R'(1+f/2) \sin 2\alpha \cos^2 \beta \\ \Delta C_{23} &= C_{P_3} - C_{P_6} = 2R'(1+f/2) [ 3 \cos \alpha \sin 2\beta + \sin 2\alpha \cos^2 \beta ] \\ \Delta C_{32} &= C_{P_2} - C_{P_5} = 2R'(1+f/2) [ 3 \cos \alpha \sin 2\beta - \sin 2\alpha \cos^2 \beta ] \end{aligned} \quad (6)$$

These three pressure coefficients can be combined into a coefficient that is mainly dependent on the flow angle  $\alpha$  and another coefficient that is mainly dependent on the flow angle  $\beta$  as follows:

$$\begin{aligned} \Delta C_A &= \frac{2\Delta C_1 + \Delta C_2 - \Delta C_3}{3} = 4R'(1+f/2) \sin 2\alpha \cos^2 \beta \\ \Delta C_B &= \frac{\Delta C_2 + \Delta C_3}{\sqrt{3}} = 4R'(1+f/2) \cos \alpha \sin 2\beta \end{aligned} \quad (7)$$

The sensitivity to changes in flow angle is defined as  $\frac{\partial \Delta C}{\partial \alpha}$  or  $\frac{\partial \Delta C}{\partial \beta}$ . These are given by

$$\frac{\partial \Delta C_A}{\partial \alpha} = 8R'(1+f/2) \cos 2\alpha \cos^2 \beta$$

$$\frac{\partial \Delta C_B}{\partial \alpha} = -4R'(1+f/2) \sin \alpha \cos 2\beta$$

With a given flow angle  $\alpha$ , the sensitivity to changes in flow angle  $\beta$  is given by  $\frac{\partial \Delta C}{\partial \beta}$ . These are given by

Also, the sensitivity is proportional to the slope of the probe's surface,  $R'$ . Equation 8 is plotted in Figure 4 for  $f=0$ . It is quite apparent from the figure that the probe angularity sensitivity -- regardless of shape -- depends on  $\alpha$  and  $\beta$ . Approximately a 10% reduction in sensitivity occurs for  $\alpha$  and  $\beta$  values of  $10^\circ$ . Note that  $\partial \Delta C_\alpha / \partial \alpha$  is the same for both positive and negative values of  $\alpha$  and  $\beta$ .

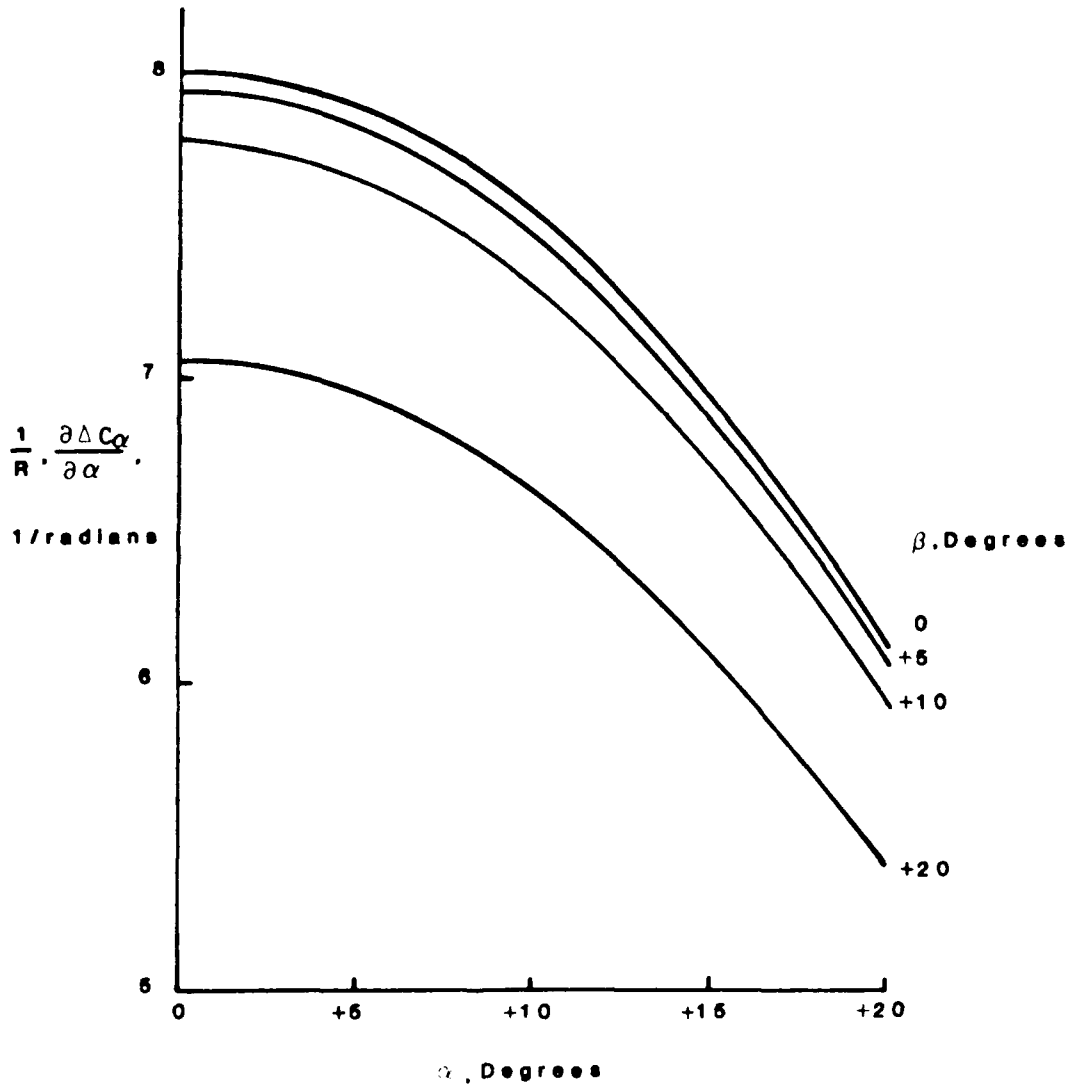


Figure 4. PROBE ANGULAR SENSITIVITY AS A FUNCTION OF  $\alpha$  AND  $\beta$  (REF. 18)

The average pressure coefficient can be used to determine the flow-field static pressure,  $P_\infty$ .  $C_p$  is evaluated at a number of theta values and the results summed and divided by the number of theta values. For the seven-hole probe of Figure 3, this process yields

$$\langle C_p \rangle = [1 - f - f^2/4 + (R')^2] \cos^2 \alpha \cos^2 \beta - [1 + 2(R')^2] \quad (10)$$

Huffman developed an expression for a quasi total pressure from his analysis by integrating the pressure over the body surface, resolving this force into an axial component, and dividing by the cross sectional area. His relationship is

$$\langle C_p \rangle_z = \frac{\cos^2 \alpha \cos^2 \beta}{R_l^2} \int_0^l (R')^2 [f + f^2/4 + (R')^2] dz - \sin^2 \beta - \sin^2 \alpha \cos^2 \beta \quad (11)$$

where  $l$  denotes the integration length.

For a conical shaped body,  $R'$  is constant and Equation 11 reduces to

$$\langle C_p \rangle_z = [1 - f - f^2/4 - (R')^2] \cos^2 \alpha \cos^2 \beta - 1 \quad (12)$$

A probe pressure coefficient that is proportional to the dynamic pressure can be obtained by subtracting Equation 12 from Equation

$$\langle C_p \rangle_z = 2(R')^2 [1 - \cos^2 \alpha \cos^2 \beta] \quad (13)$$

Some insight into probe calibration can be obtained by studying the plot of  $\alpha$  and  $\beta$  versus  $\Delta C_a$  and  $\Delta C_b$  in Figure 5, the plot of  $\langle C_p \rangle$  versus  $\alpha$  and  $\beta$  in Figure 6, the plot of  $\langle C_p \rangle_z$  versus  $\alpha$  and  $\beta$  in Figure 7, and the plot of  $[\langle C_p \rangle_z - \langle C_p \rangle]$  versus  $\alpha$  and  $\beta$  in Figure 8. Figures 5 through 8 were calculated for  $R' = .268$  and  $f = 0$ . Note the near linear relation between each angle and its respective pressure coefficient as shown in Figure 5. Also, the nearly circular contours of constant  $\langle C_p \rangle$ ,  $\langle C_p \rangle_z$ , and  $[\langle C_p \rangle_z - \langle C_p \rangle]$  as shown in Figures 6, 7, and 8, respectively. Probe manufacturing imperfection and angular misalignment of the pressure ports will cause these curves to become somewhat distorted.

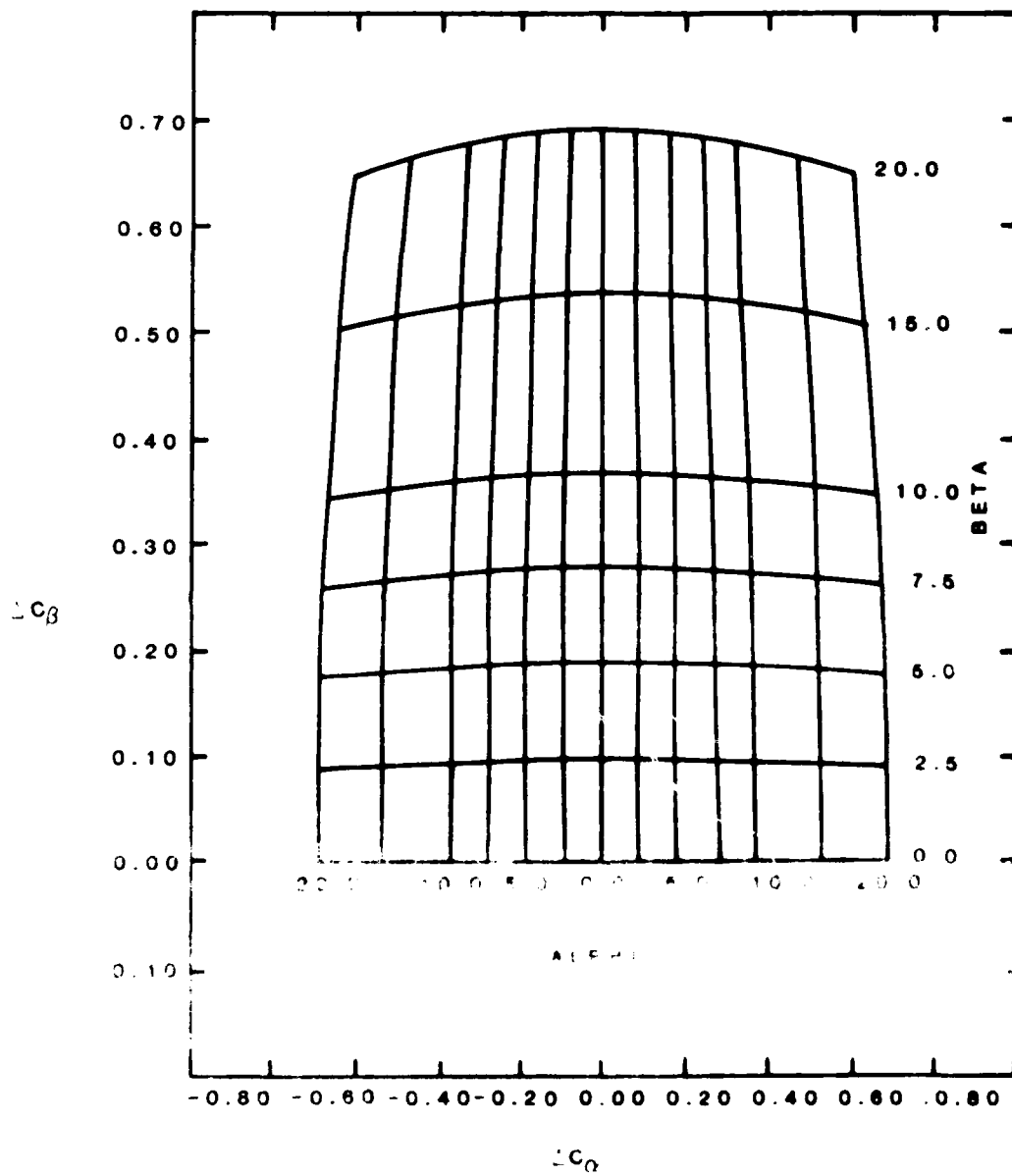


Figure 5.  $\beta$  VERSUS  $\alpha$  FOR A TYPICAL FLOW DIRECTION PROBE (REF 18)

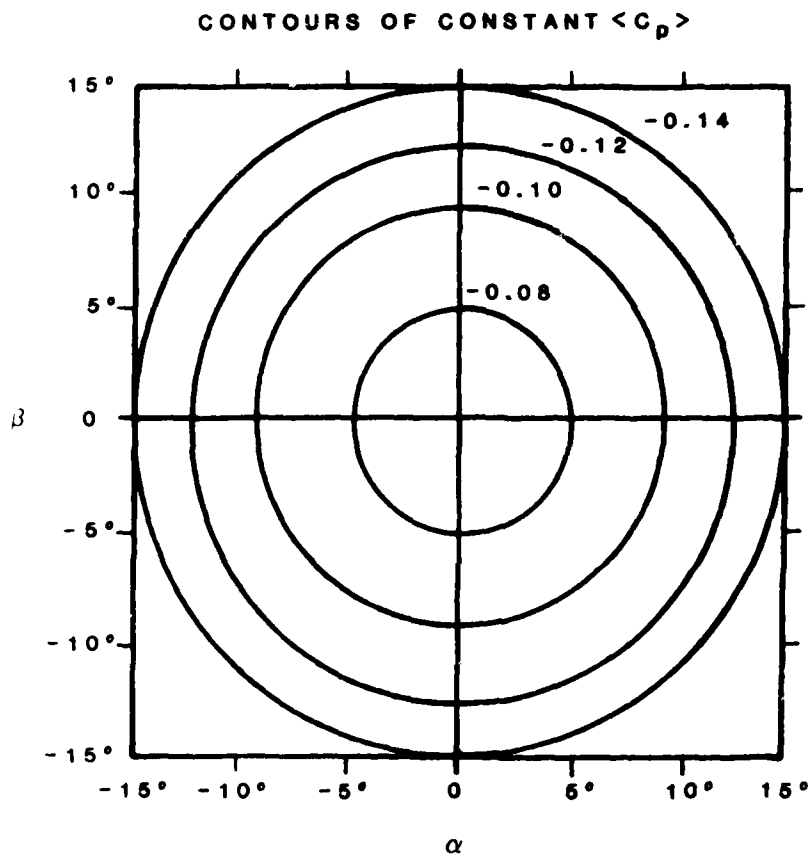


Figure 6. CONTOURS OF CONSTANT  $\langle C_p \rangle$

CONTOURS OF CONSTANT  $\langle C_p \rangle_z$

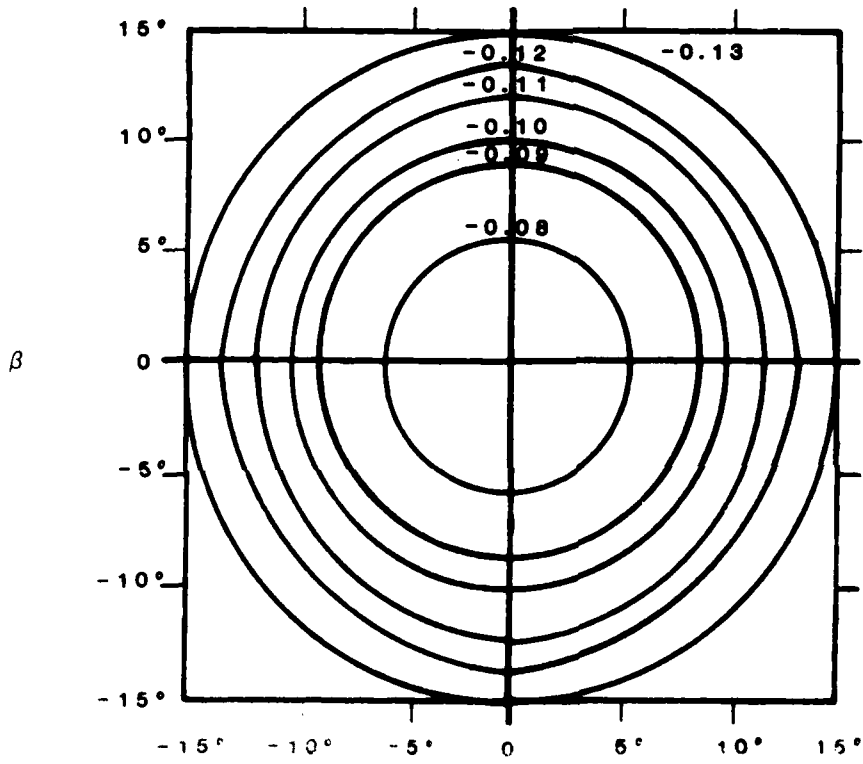


Figure 7. CONTOURS OF CONSTANT  $\langle C_p \rangle_z$

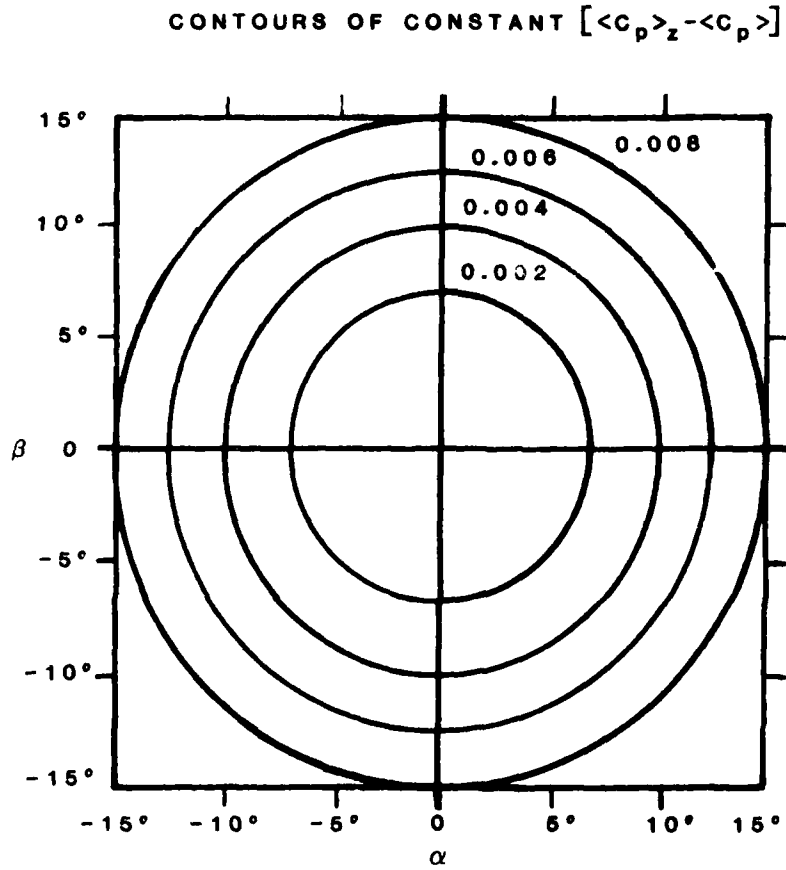


Figure 8. CONTOURS OF CONSTANT  $\langle C_p \rangle_z - \langle C_p \rangle$

### C. Seven-Hole Probe Design

The seven-hole probe is characterized by six periphery ports surrounding one central port (Fig. 9). The probe is constructed by packing seven properly sized stainless steel tubes into a stainless steel casing. For the current probe used at the Air Force Academy, the inner seven tubes have an outside diameter of .028 inches with a .005-inch wall thickness. Once assembled in the order shown below, the tubes are soldered together and machined to the desired half angle  $\epsilon$  (usually 25 or 30 degrees) at the tip (Ref. 2). It should be noted that the manufacture of seven-hole probes (versus four/five hole probes) is much simpler due to this packing arrangement.

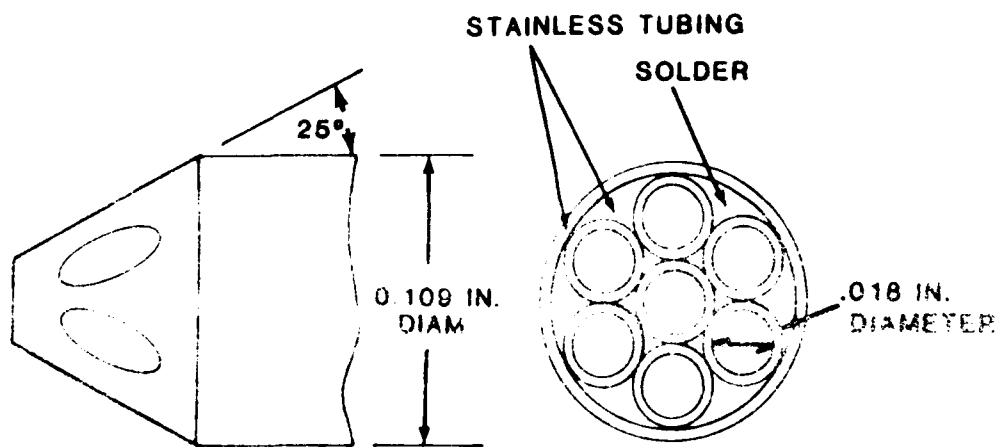


Figure 9. PROBE GEOMETRY

### III. Seven-Hole Probe Calibration Theory

Because of their small size and individual construction, all probes have inherent manufacturing defects that require the unique calibration of each probe. Gallington (Ref. 24) developed the calibration theory required for incompressible, uniform flows. His power series method produces explicit polynomial expressions for the desired aerodynamic properties and is easily programmed. The following section presents a synopsis of Gallington's scheme for incompressible, uniform flow calibration as presented by Gallington (Ref. 24) and by Gerner and Maurer (Ref 2).

#### A. Low Versus High Flow Angles, Incompressible Flow

In this calibration technique for incompressible, uniform flow, the probe face is divided into two sectors. The inner flow sector deals with low flow angles in which the angle between the probe's axis and the freestream velocity vector is less than 30 degrees. The other or outer sector deals with high flow angles of over 30 degrees. Thirty degrees is the dividing point because flow typically begins to detach over the top surface of the probe tip around this local flow angle. The hole numbering system used for both sectors and the remainder of the report is as follows:

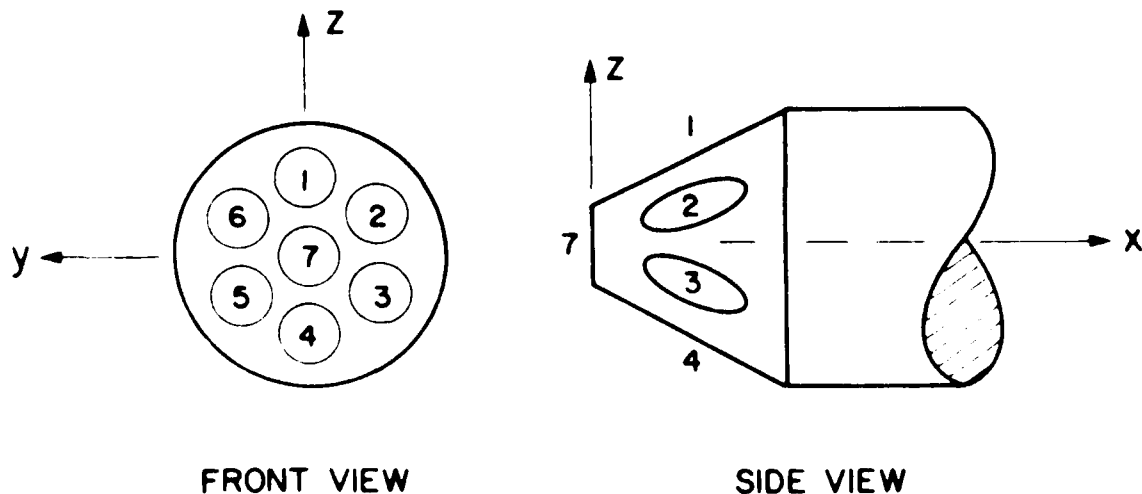
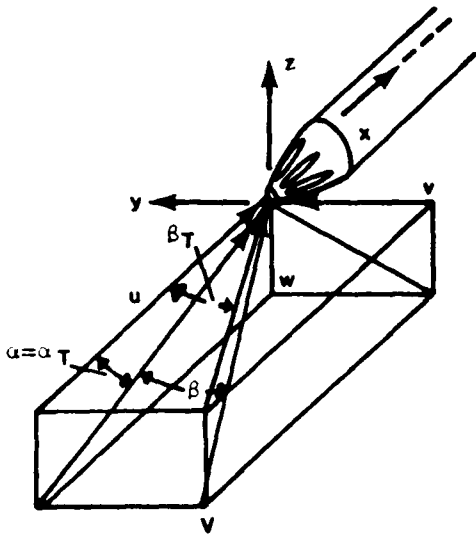


Figure 10. PORT NUMBERING CONVENTION AND PRINCIPAL AXES

The x-axis is defined to be positive in the unperturbed freestream flow direction. The origin is a point at the tip of the cone formed by the probe (Fig. 10).

#### B. Probe Axis System for Low Flow Angles

The axis system for low flow angles is the tangential alpha-beta system depicted below (Fig. 11). The angle of attack, alpha ( $\alpha_T$ ), is measured directly as the projection on the x-plane. To preserve symmetry, the angle of sideslip ( $\beta_T$ ) is measured directly as the projection on the y-plane.



CONVENTIONAL	TANGENT
$u = V \cos \alpha \cos \beta$	$\alpha_T = \arctan \frac{w}{u}$
$v = V \sin \beta$	$\beta_T = \arctan \frac{v}{u}$
$w = V \sin \alpha \cos \beta$	

Figure 11. LOW ANGLE REFERENCE SYSTEM

#### 1. Pressure Coefficients for Low Flow Angles

The flow angle is determined as a function of dimensionless pressure coefficients. Three pairs of opposing peripheral ports measure the differences in pressure from one side of the probe to the other in: form the following three relationships:

$$C_{p1} = \frac{P_4 - P_1}{P_\infty - P_1 - c} \quad , \quad C_{p12} = \frac{P_3 - P_1}{P_7 - P_1 - c} \quad , \quad C_{p13} = \frac{P_2 - P_1}{P_7 - P_1 - c} \quad (10)$$

As the numerator measures changes in flow angularity, the denominator nondimensionalizes the expression with the apparent dynamic pressure. The center port pressure,  $P_7$ , approximates the local total pressure while the average of the circumferential port pressures  $\bar{P}_{1-6}$  approximates the local static pressure. To transform these pressure coefficients to the tangential reference system, Gallington (Ref. 24) formulates the following relationships:

$$C_\alpha = \frac{1}{3} (2C_{\alpha_1} + C_{\alpha_2} - C_{\alpha_3}) \quad , \quad C_\beta = \frac{1}{\sqrt{3}} (C_{\alpha_2} + C_{\alpha_3}) \quad (15)$$

It is important to realize that  $C_\alpha$  and  $C_\beta$  are not independent of each other; that is,  $C_\alpha$  is a function of all six peripheral ports while  $C_\beta$  is a function of all but ports 1 and 4.

Besides the two angular pressure coefficients, two other low angle pressure coefficients,  $C_o$  and  $C_q$ , are defined in Gallington's work (Ref. 24):

$$C_o = \frac{P_7 - P_{oL}}{P_7 - \bar{P}_{1-6}} \quad , \quad C_q = \frac{P_7 - \bar{P}_{1-6}}{P_{oL} - P_{\infty L}} \quad (16)$$

$C_o$  is the apparent total pressure coefficient with respect to each hole and is a means to convert actual pressures measured by the probe to accurate values of local total pressure. The numerator measures the difference between the approximate total pressure measured by the center port  $P_7$  and the actual local total pressure  $P_{oL}$ . As with the previous coefficients, the denominator nondimensionalizes the expression with the apparent local dynamic pressure.

The velocity pressure coefficient,  $C_q$ , serves a similar conversion function as  $C_o$  except that it relates the probe

pressures to the actual dynamic pressure. The numerator in this coefficient represents the probe's approximation of the local dynamic pressure while the denominator represents the actual dynamic pressure of the freestream test conditions.

#### B. Probe Axis System for High Flow Angles

The real advantage of using the non-nulling seven-hole probe over other multi-hole probes appears in the ability to measure high-angle flows. At high angles of attack (greater than 30 degrees), the flow detaches over the upper surface of the probe, and pressure ports in the separated wake are insensitive to small changes in flow angularity (Fig. 12).

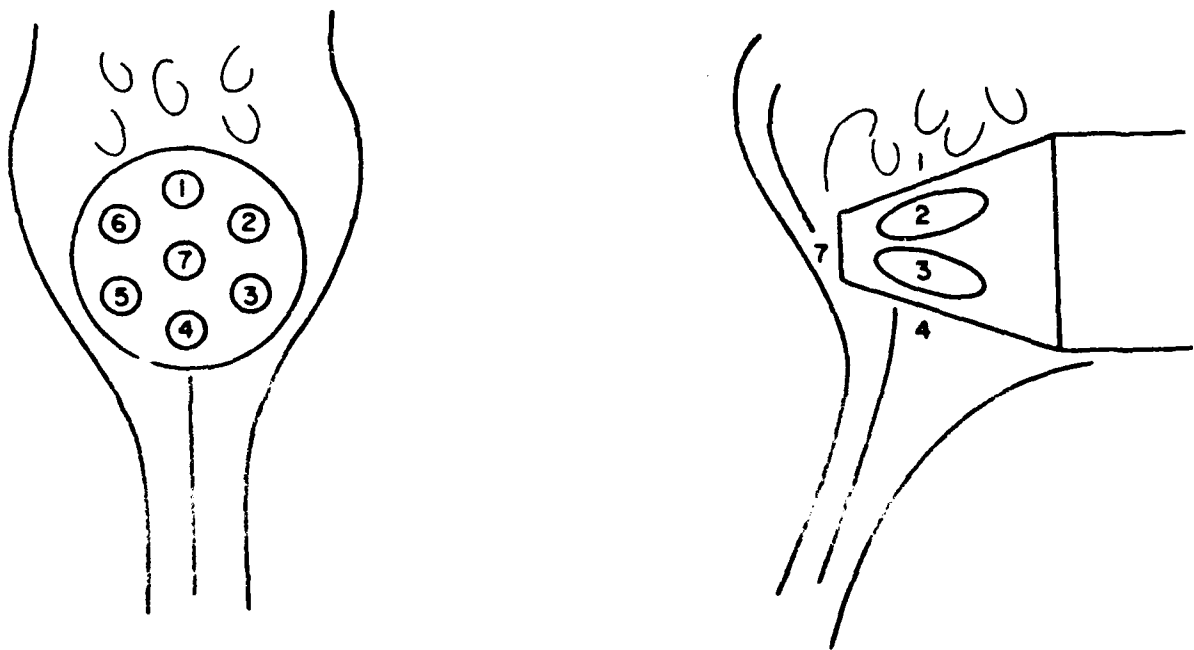
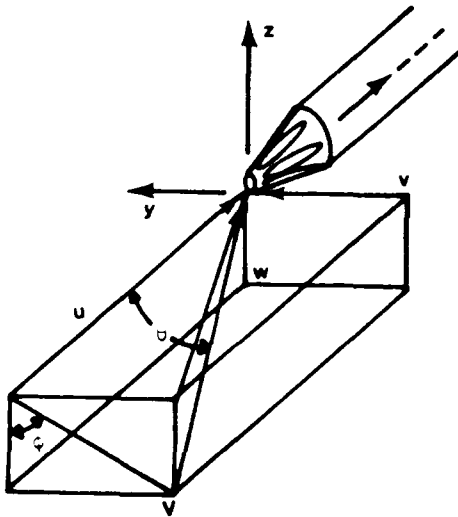


Figure 12. FLOW PATTERN OVER SEVEN-HOLE PROBE AT HIGH ANGLE OF ATTACK

Consequently, high angle measurements must only be made from ports in the attached flow. Five-hole and other pressure probes have been ineffective in this regime due to this flow separation and lack of sensing ports in the attached flow region. The seven-hole probe avoids this problem because at least three ports remain in the attached flow region, allowing sufficient data to be recorded to document the flow angle.

According to Gallington, the tangential reference system is inappropriate at high flow angles because of indeterminate angles and singularities (Ref. 24). Instead, the polar reference system is used (Fig. 13) where  $\theta$  represents the pitch angle and  $\phi$  represents the roll angle.



POLAR	TANGENT
$u = V \cos \theta$	$\alpha_T = \arctan \frac{w}{u}$
$v = V \sin \theta \sin \phi$	$\beta_T = \arctan \frac{v}{u}$
$w = V \sin \theta \cos \phi$	

Figure 13. HIGH ANGLE REFERENCE SYSTEM

More specifically,  $\theta$  denotes the angle that the velocity vector forms with respect to the probe's x-axis, and  $\phi$  signifies the azimuthal orientation of the velocity vector in the y-z plane. We should note that a positive  $\phi$  is measured counterclockwise from the the negative z axis when the probe is viewed from the front.

Based on Gallington's original work with the seven-hole probe at high angles of attack, Gerner and Mauer accomplished the following analysis (Ref 2). Kuethe and Chow's Foundations of Aerodynamics: Bases of Aerodynamic Design, explains that the separation points of a cylinder in turbulent flow are over 100 degrees from the frontal stagnation point. Flow around a conical body such as a probe tip was likely to remain attached longer, and the u-velocity component was prone to extend the separation points downstream even further. Therefore, for the high angle flow shown in Figure 14, ports 3, 4, 5, and 7 lie in attached flow, and port 1 lies in separated flow. The flow over ports 2 and 6 is unpredictable, and their readings are discarded (Ref. 2).

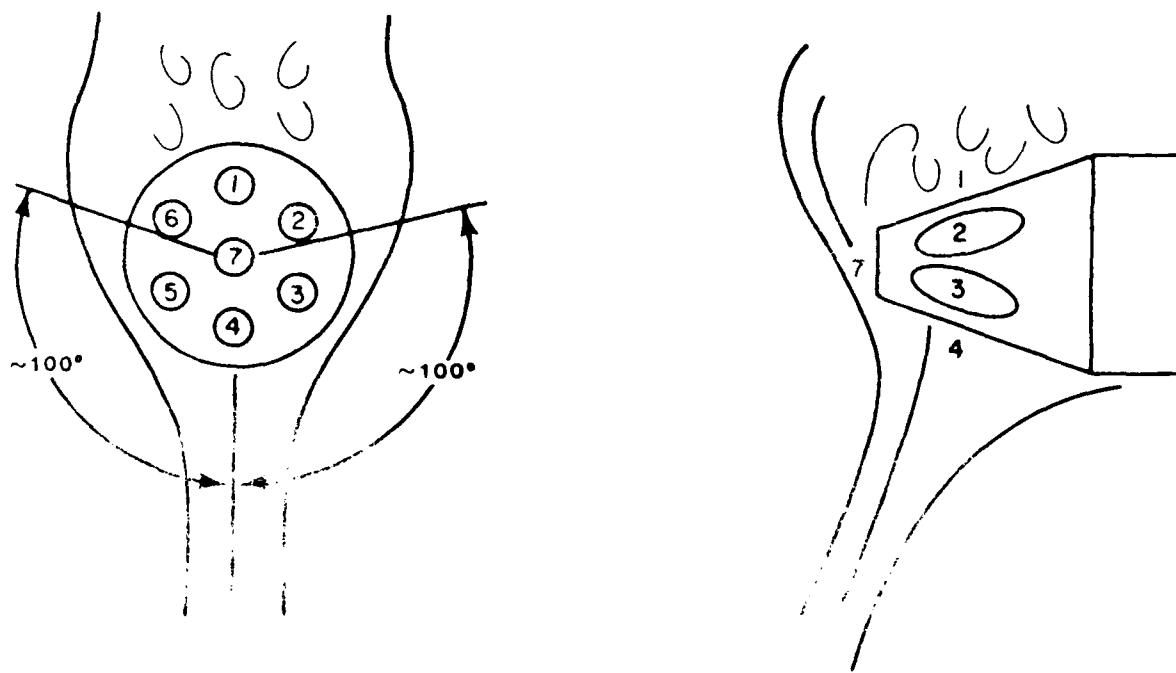


Figure 14. FLOW OVER PROBE AT HIGH ANGLE OF ATTACK

#### Flow over a Seven-Hole Probe at High Flow Angles

Flow over a seven-hole probe at high flow angles is characterized by separated flow. The pressure coefficients are low and the velocity is high.

pressure differences. Unlike low flow angles, however, the center port pressure is now the most dependent port on local flow angle. Consequently, a pitch angular pressure coefficient should measure the difference between the center port and a new stagnation port. In the example below, the pressure at  $P_4$  approximates the local total pressure.

$$C_{O_4} = \frac{P_4 - P_7}{P_4 - \frac{P_3 + P_5}{2}} \quad (17)$$

The expression is again nondimensionalized by the apparent dynamic pressure. The average of  $P_3$  and  $P_5$  approximates the static pressure and is relatively independent to changes in roll.

Although the average is independent of  $\phi$ , the difference is sensitive to roll angle. As the probe's azimuthal orientation changes, the windward pressure rises and the leeward pressure falls. The result is a roll angular pressure coefficient (example for port 4 is Equation 8 below) that is also nondimensionalized by the apparent dynamic pressure.

$$C_{\phi_4} = \frac{P_3 - P_5}{P_4 - \frac{P_3 + P_5}{2}} \quad (18)$$

The high flow angle  $C_O$  and  $C_Q$  coefficients are translated from their low flow angle counterparts using the same rationale found in the development of  $C_\psi$  and  $C_\phi$ . The low angle  $C_O$  and  $C_Q$  coefficients are changed to account for the different ports that represent total and static pressures in the high-angle regime. The equations for  $C_\psi$ ,  $C_\phi$ ,  $C_O$ , and  $C_Q$  are as follows:

$$C_{\Theta_1} = \frac{P_1 - P_7}{P_1 - \frac{P_2 + P_6}{2}}$$

$$C_{\phi_1} = \frac{P_6 - P_2}{P_1 - \frac{P_6 + P_2}{2}}$$

$$C_{\Theta_2} = \frac{P_2 - P_7}{P_2 - \frac{P_1 + P_3}{2}}$$

$$C_{\phi_2} = \frac{P_1 - P_3}{P_2 - \frac{P_1 + P_3}{2}}$$

$$C_{\Theta_3} = \frac{P_3 - P_7}{P_3 - \frac{P_2 + P_4}{2}}$$

$$C_{\phi_3} = \frac{P_2 - P_4}{P_3 - \frac{P_2 + P_4}{2}}$$

$$C_{\Theta_4} = \frac{P_4 - P_7}{P_4 - \frac{P_3 + P_5}{2}}$$

$$C_{\phi_4} = \frac{P_3 - P_5}{P_4 - \frac{P_3 + P_5}{2}}$$

$$C_{\Theta_5} = \frac{P_5 - P_7}{P_5 - \frac{P_4 + P_6}{2}}$$

$$C_{\phi_5} = \frac{P_4 - P_6}{P_5 - \frac{P_4 + P_6}{2}}$$

$$C_{\Theta_6} = \frac{P_6 - P_7}{P_6 - \frac{P_5 + P_1}{2}}$$

$$C_{\phi_6} = \frac{P_5 - P_1}{P_6 - \frac{P_5 + P_1}{2}}$$

(19)

$$C_{o1} = \frac{P_1 - P_{oL}}{P_1 - \frac{P_2 + P_6}{2}}$$

$$C_{o2} = \frac{P_2 - P_{oL}}{P_2 - \frac{P_3 + P_1}{2}}$$

$$C_{o3} = \frac{P_3 - P_{oL}}{P_3 - \frac{P_4 + P_2}{2}}$$

$$C_{o4} = \frac{P_4 - P_{oL}}{P_4 - \frac{P_5 + P_3}{2}}$$

$$C_{o5} = \frac{P_5 - P_{oL}}{P_5 - \frac{P_6 + P_4}{2}}$$

$$C_{o6} = \frac{P_6 - P_{oL}}{P_6 - \frac{P_1 + P_5}{2}}$$

$$C_{q1} = \frac{P_1 - \frac{P_2 + P_6}{2}}{P_{oL} - P_{\infty L}}$$

$$C_{q2} = \frac{P_2 - \frac{P_3 + P_1}{2}}{P_{oL} - P_{\infty L}}$$

$$C_{q3} = \frac{P_3 - \frac{P_4 + P_2}{2}}{P_{oL} - P_{\infty L}}$$

$$C_{q4} = \frac{P_4 - \frac{P_5 + P_3}{2}}{P_{oL} - P_{\infty L}}$$

$$C_{q5} = \frac{P_5 - \frac{P_6 + P_4}{2}}{P_{oL} - P_{\infty L}}$$

$$C_{q6} = \frac{P_6 - \frac{P_1 + P_5}{2}}{P_{oL} - P_{\infty L}}$$

(20)

F. Division of Angular Space

The most obvious difference between low and high pressure coefficients is that six high coefficients are needed for the high angles. This fact leads to the question of what factors determine when a certain set of coefficients should be employed. Gallington proposes the "division of angular space" shown in Figure 15 (Ref. 24).

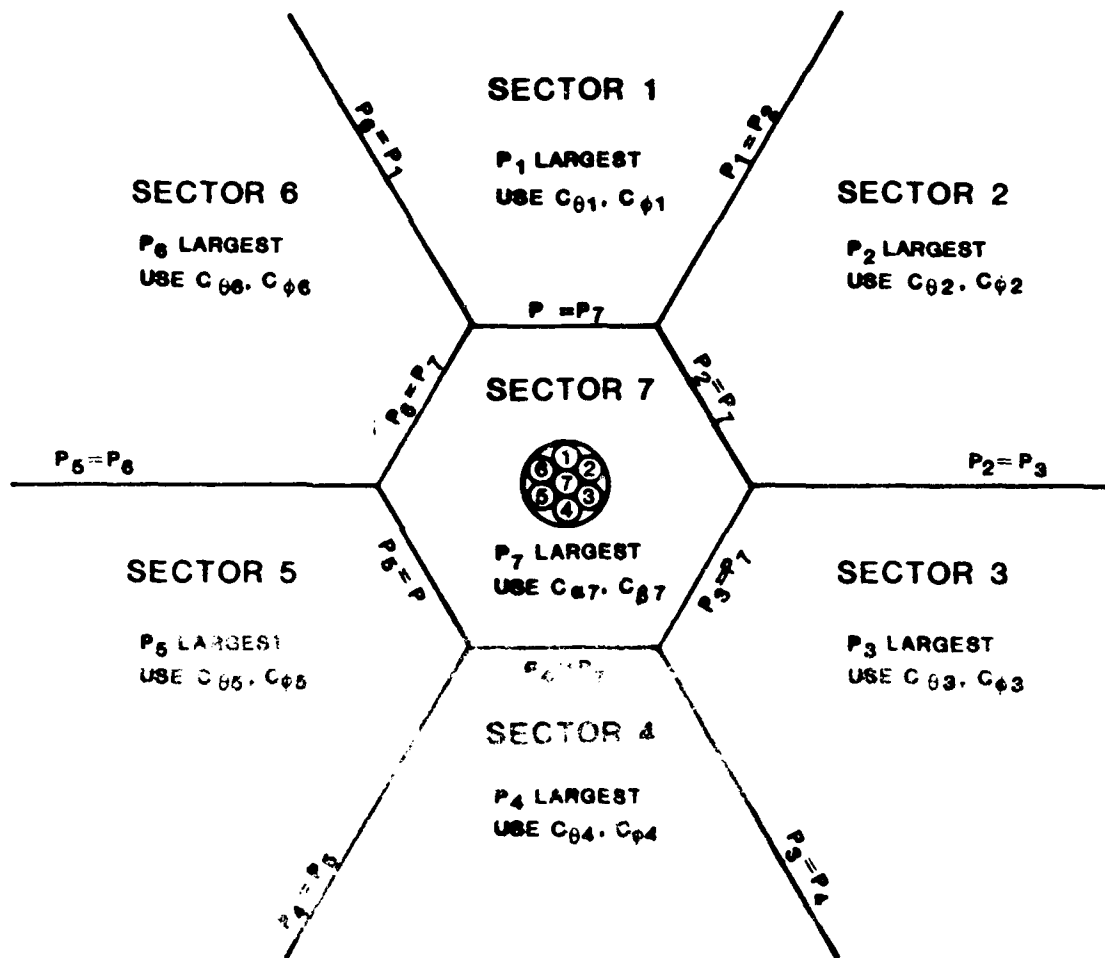


Figure 15. DIVISION OF ANGULAR SPACE

This method separates probe measurements into seven sectors -- a central low angle sector and six circumferential high angle sectors. Data points are placed in a given sector based on the highest port pressure measured on the probe.

#### G. Polynomial Power Series Expansion

Once the pressure coefficients are calculated, they must be converted to  $\alpha_T, \beta_T, C_o,$  or  $C_q$  for low angle flows and  $\theta, \phi, C_o,$  or  $C_q$  for high angle flows. This conversion is accomplished by solving the following fourth order power series:

	<u>Order of Terms</u>
$A_1 = K_1^A +$	0th
$K_2^A C_{\alpha_1} + K_3^A C_{\beta_1} +$	1st
$K_4^A C_{\alpha_1}^2 + K_5^A C_{\alpha_1} C_{\beta_1} + K_6^A C_{\beta_1}^2 +$	2nd (21)
$K_7^A C_{\alpha_1}^3 + K_8^A C_{\alpha_1}^2 C_{\beta_1} + K_9^A C_{\alpha_1} C_{\beta_1}^2 + K_{10}^A C_{\beta_1}^3 +$	3rd
$K_{11}^A C_{\alpha_1}^4 + K_{12}^A C_{\alpha_1}^3 C_{\beta_1} + K_{13}^A C_{\alpha_1}^2 C_{\beta_1}^2 + K_{14}^A C_{\alpha_1} C_{\beta_1}^3 + K_{15}^A C_{\beta_1}^4$	4th

"A" signifies the desired output quantity with the subscript denoting the ith such quantity. "K" denotes the presently unknown calibration coefficients. The calibration process entails finding these calibration coefficients with the A's as known conditions and the C's as measured pressure coefficients at these known conditions.

## B. Determination of Calibration Coefficients

Rewriting in matrix notation for n terms, the power series becomes

$$\begin{bmatrix} A_1 \\ A_2 \\ A_3 \\ \dots \\ A_n \end{bmatrix} = \begin{bmatrix} 1 & C_{\alpha_1} & C_{\beta_1} & C_{\alpha_1}^2 & C_{\alpha_1} & C_{\beta_1} & C_{\beta_1}^2 & \dots & C_{\beta_1}^4 \\ 1 & C_{\alpha_2} & C_{\beta_2} & C_{\alpha_2}^2 & C_{\alpha_2} & C_{\beta_2} & C_{\beta_2}^2 & \dots & C_{\beta_2}^4 \\ 1 & C_{\alpha_3} & C_{\beta_3} & C_{\alpha_3}^2 & C_{\alpha_3} & C_{\beta_3} & C_{\beta_3}^2 & \dots & C_{\beta_3}^4 \\ \dots & \dots \\ 1 & C_{\alpha_n} & C_{\beta_n} & C_{\alpha_n}^2 & C_{\alpha_n} & C_{\beta_n} & C_{\beta_n}^2 & \dots & C_{\beta_n}^4 \end{bmatrix} \begin{bmatrix} K_1^A \\ K_2^A \\ K_3^A \\ \dots \\ K_n^A \end{bmatrix} \quad (22)$$

or simply

$$[A] = [C] [K] \quad (23)$$

Solving for  $[K]$  by the least squares curve fit outlined by Netter and Wasserman in Gallington (Ref. 24), the following is obtained:

$$[K] = [C^T C]^{-1} [C^T] [A] \quad (24)$$

With known calibration coefficients, the probe can be used to determine output quantities ( $\alpha_T, \beta_T, \dots, C_{\alpha_n}, C_{\beta_n}, \dots, \phi_n$ ) for any given  $\psi_n$  for an unknown flow field. It is assumed at this point that to this point the flow field has been uniform and steady-state. Temperature or velocity gradients have not been accounted for. Finally, while the local total and dynamic pressures are not found explicitly from the power series, they are

easily determined by substituting  $C_o$  and  $C_q$  into Equation 16 (low angles) or Equation 20 (high angles).

#### 1. Extension to Compressible Flows

Gerner and Maurer (Ref. 2) expanded the technique to subsonic compressible flows with the introduction of a nondimensional pressure coefficient representative of compressibility effects. This coefficient,  $C_M$ , had to become insignificant at very low Mach numbers; thus, any terms bearing  $C_M$  in the power series expansion would have to approach zero as Mach approached zero. This would leave essentially an incompressible power series with the regular two angular pressure coefficients as previously described. Because pressure probes are unable to determine Mach number in the hypersonic range,  $C_M$  had to approach a finite limit at very high Mach numbers. Consequently, large changes of Mach numbers in this region would have negligible effect on the compressibility coefficient.

Gerner and Maurer (Ref. 2) found that these requirements were satisfied by the apparent dynamic-to-total-pressure ratio (low angles).

$$C_M = \frac{P_7 - \bar{P}_1 - 6}{P_7} \quad (25)$$

Similarly, for high angle flow, the compressibility coefficient in each sector is:

$$C_{M_1} = \frac{P_1 - \frac{P_6 + P_2}{2}}{P_1}$$

$$C_{M_2} = \frac{P_2 - \frac{P_1 + P_3}{2}}{P_2}$$

$$C_{M_3} = \frac{P_3 - \frac{P_2 + P_4}{2}}{P_3}$$

$$C_{M_4} = \frac{P_4 - \frac{P_3 + P_2}{2}}{P_4}$$

$$C_{M_5} = \frac{P_5 - \frac{P_4 + P_6}{2}}{P_5}$$

$$C_{M_6} = \frac{P_6 - \frac{P_5 + P_1}{2}}{P_6}$$

One of the primary problems of extending the seven-hole probe's capabilities into compressible flow lies in the mathematics. First, by adding a third coefficient to the fourth order power series, the number of terms and hence calibration coefficients jumps from 15 to 35. Gerner and Maurer say that approximately 80 data points in two variables ( $C_\alpha$  and  $C_\beta$ ) for each of the seven sectors are needed for a complete incompressible calibration. That fact results in 560 data points, and the addition of a Mach number compressibility coefficient makes the data set unwieldy (Ref. 2). These two factors create complex and time consuming matrix operations. Additionally, the amount of run time needed to operate the wind tunnel for all of the calibration data points is prohibitive as well as costly.

Gerner and Maurer suggest a two-part solution to make the addition of  $C_M$  feasible. By reducing the fourth order power series to a third order, the number of calibration coefficients is reduced to 20. Gerner and Maurer also decrease the number of data points required for calibration by employing a 6x6 Latin Square technique (Ref. 2) for purposes of obtaining calibration data. The Latin Square is a numerical method that ensures a homogeneous, random sample of a three-dimensional probability space.

Seven-hole probe work incorporating these two changes results in the following conclusions for compressible flow. The third order polynomial does not accurately represent the parameter dependence on Mach number and degree of pitch. Next, based on statistically significant differences between the standard deviations of experimental calibration and the complete calibration, Latin

Squares produce a sample which accurately represents a very large three-dimensional parameter space.

With these changes, the seven-hole probe may now be used in an unknown uniform, compressible flow. Since the seven-hole probe has never been subjected to supersonic applications, no shocks will lie ahead of the probe, and the isentropic flow relationship is employed to find Mach number (Ref. 2).

$$M_o = \frac{2}{\gamma - 1} \left( \left[ 1 - \frac{P_o - P_{\infty}}{P_o} \right]^{\frac{\gamma - 1}{\gamma}} - 1 \right) \quad (27)$$

Knowing  $C_o$ ,  $C_q$ , and the seven port pressures, the local Mach number may be determined explicitly from the dynamic to total pressure ratio. This ratio for the inner sector is represented in Equation 28 below (Ref. 2).

$$\frac{P_{oL} - P_{\infty L}}{P_{oL}} = [C_q \left( \frac{P_7}{P_7 - P_{1-6}} - C_o \right)]^{-1} \quad (28)$$

Similar equations for the outer sectors may be derived, using the appropriate port pressures for approximate total and dynamic pressures.

#### IV. Seven-Hole Probe in Shear Flow

Under the present calibration scheme, the existence of a velocity gradient in the flow will cause the probe to measure an erroneous uniform flow at fictitious flow angle. For example, a flow having the properties  $M=.3, \alpha=0^\circ, \beta=0^\circ$ , with a velocity gradient (Fig.16) might cause the probe to "think" that it sees a flow with a certain angularity, say  $\beta=10^\circ$  (see Fig. 17).

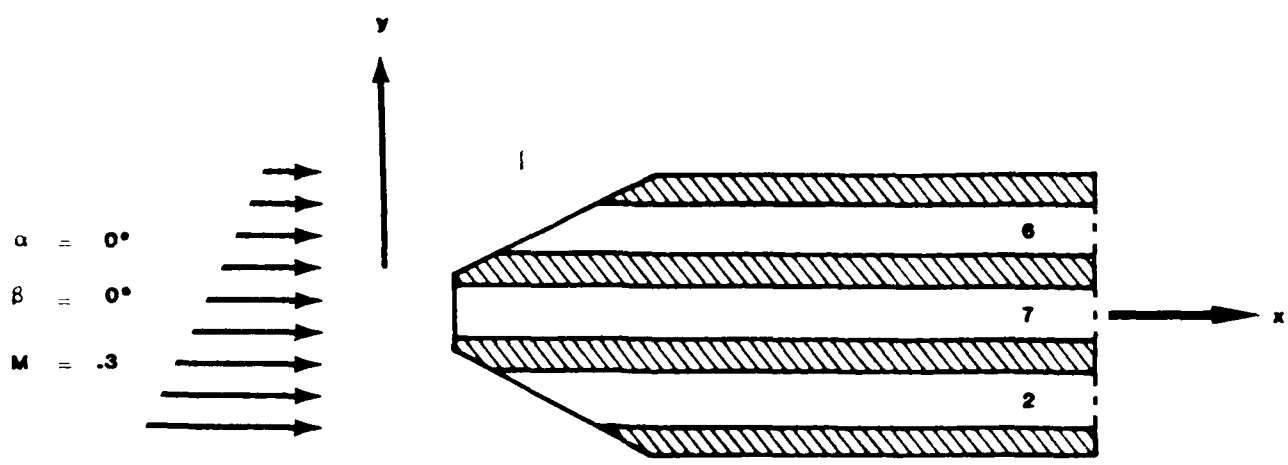


Figure 16. ACTUAL FLOW CONDITION

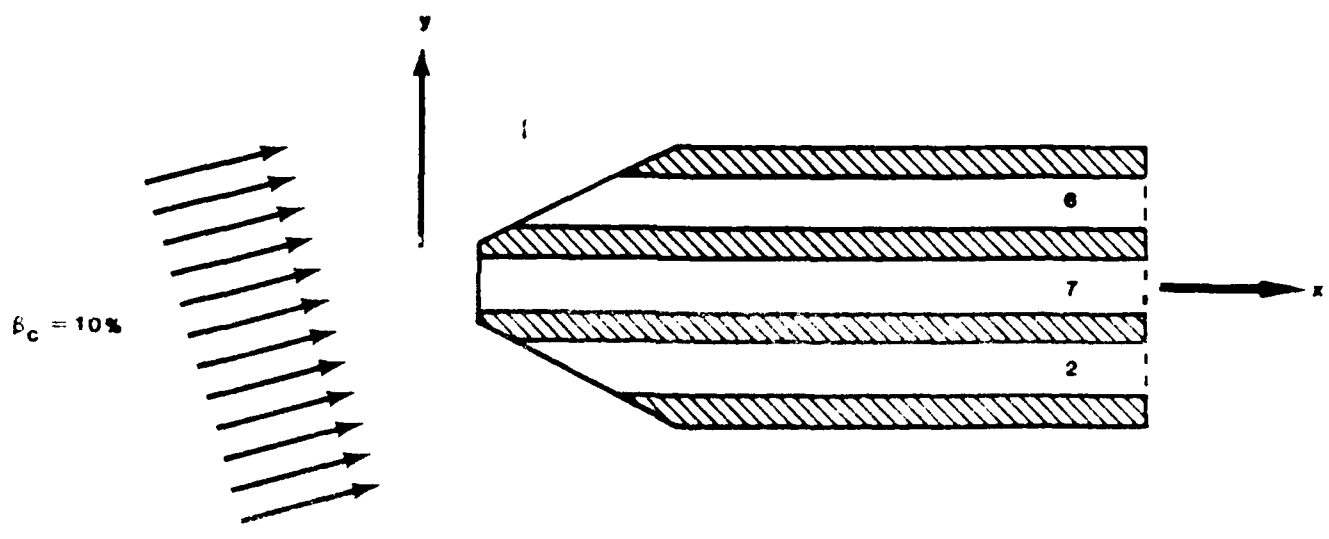


Figure 17. APPARENT FLOW CONDITION

The probe has seven ports, each with a different pressure coefficient, all seven values compute a single velocity, independent of angle. The use of these eight ports in a uniform flow cell either produces an apparent flow condition that does not truly represent the actual flow or, if the probe is used in a uniform flow cell, it will produce a velocity that is

determined. Then using the "backstepping" technique developed in the following sections, the apparent measured values can be corrected to the actual flow values.

#### A. Slender Body Theory

The slender body theory developed by Huffman is utilized in this section to model flow around the probe (Ref. 20). With this model, the probe's port pressure coefficients can be estimated as a function of flow angularity. Using Huffman's method of viewing the probe as a small perturbation to an otherwise uniform stream, the pressure coefficients are determined by analytic means. Further, the model determines the variation of pressure coefficients with flow direction. Not included are viscous or flow separation effects as the theory is based on potential flow.

The body-geometry function,  $f$ , is a parameter used to define the geometric characteristics of a slender body and is given in Equation 2. Huffman incorporates the body shape function into calculations for the pressure coefficient as given by Equation 4. A simplified form of Equation 4 was used in this analysis as given below.

$$\begin{aligned}
 C_{p_{1c}} &= \cos^2 \alpha \cos^2 \beta [-f - (R')^2] + \sin^2 \beta [1 - 4 \sin^2 \theta] \\
 &+ \sin^2 \alpha \cos^2 \beta [1 - 4 \cos^2 \theta] + \cos \alpha \sin 2\beta [-2R' \cos \theta] \\
 &+ \sin 2\alpha \cos^2 \beta [-2R' \sin \theta] + \sin 2\alpha \cos \beta [4 \sin \theta \cos \theta]
 \end{aligned}
 \tag{29}$$

where  $R'$  is  $dR/dX$  with  $R$  as the radius of the probe, and  $(\theta)$  is the angle measured from the  $y$ -axis to the pressure port in question. The subscript "c" signifies that the approximation is valid for uniform incompressible flow.

The function that Huffman develops for the pressure coefficient at port 7 simplifies to Equation 30.

$$C_{p7c} = \cos^2 \alpha \cos^2 \beta - \sin^2 \beta - \sin^2 \alpha \cos^2 \beta \quad (30)$$

We must realize that slender body theory is only an approximate model of flow around the seven-hole probe. The reason for this lies stems from the conditions that the body radius is much smaller than the body length (slender body), and that it is easily applied to compressible flows. The only problem with this approach is that it assumes that the rate of change of body radius with respect to body length must be small. The seven-hole probe does not completely conform to this assumption for two reasons. First, the probe has a blunt tip with a slope discontinuity, while slender body theory assumes an aerodynamically smooth body coming to a point. Because the tip is blunt, flow disturbances originate at that tip. Second, due to the orientation of the peripheral hole surfaces, separation occurs on the probe surface at large angles of attack. Slender body theory assumes non-separated flow over the body for all flow angles. Even with these discrepancies, slender body theory is effective in predicting basic trends for coefficient variations with angle of attack. For example, the pressure coefficient at port 7 is predicted to be a function of the angle of attack and the angle of the probe surface. In a uniform flow with no flow angularity the pressure coefficient at port 7 is a function of the angle of attack and the angle of the probe surface. The coefficients of probe surfaces are a function of the angle of attack and the angle of the probe surface.

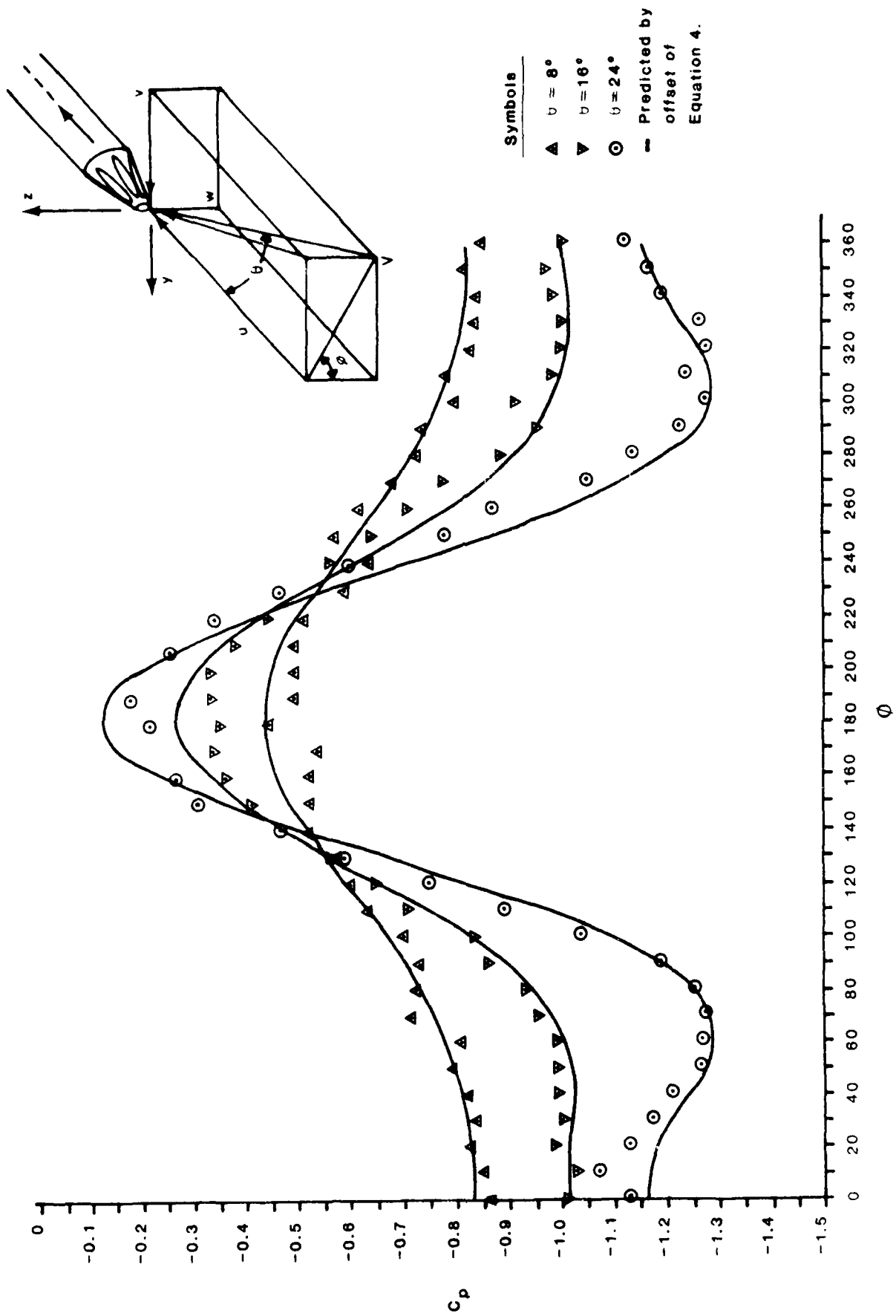


Figure 18. PREDICTED AND MEASURED  $C_p$  FOR HOLE # 1

b. The Shear Gradient

In order to work with a two-dimensional shear gradient, an alpha-beta plane is defined normal to the direction of the actual velocity and through the center point of port number 7 (Fig. 19a). The velocity at port 7 is used as a reference velocity; hence,  $v_{\alpha\beta}$  for a constant  $\alpha$  is

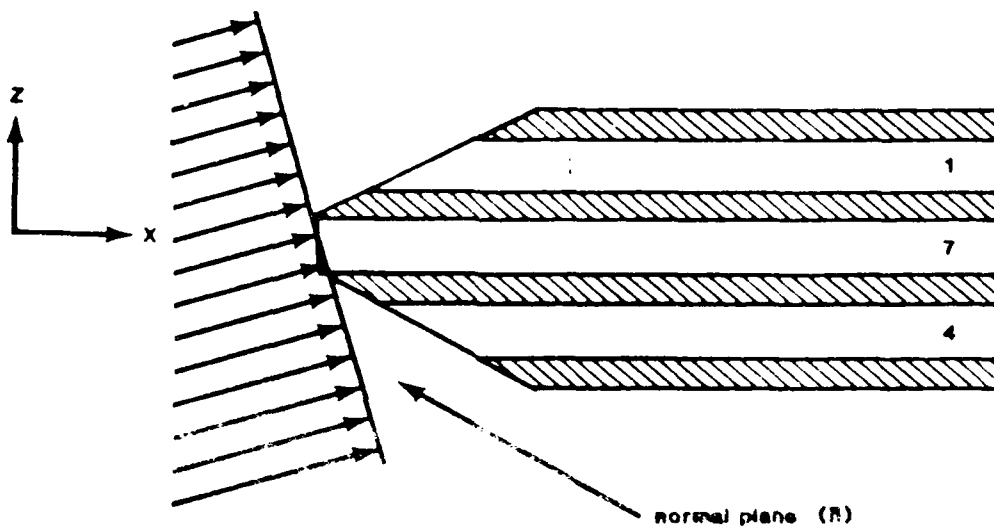


Figure 19a. SEVEN-HOLE PROBE IN A SHEAR GRADIENT

The probe is oriented such that the velocity vector at the center of port 7 is parallel to the one through port 7 and the normal plane (B) is defined normal to the direction of the actual velocity and through the center point of port number 7 (Fig. 19a). The velocity at port 7 is used as a reference velocity; hence,  $v_{\alpha\beta}$  for a constant  $\alpha$  is

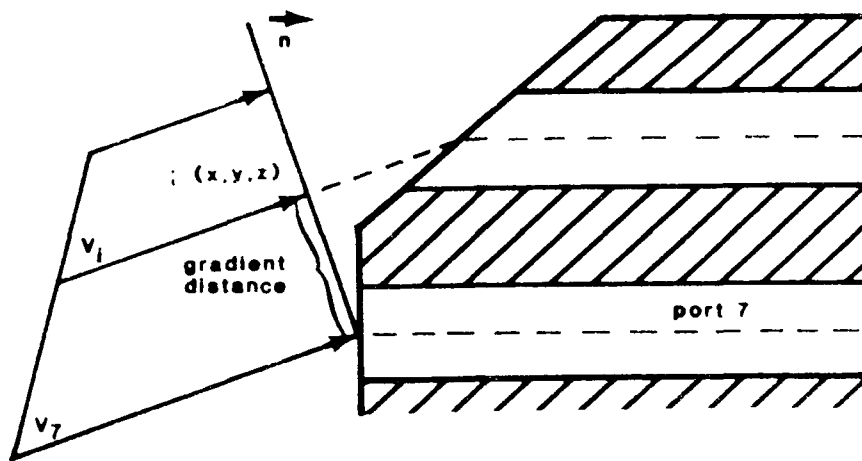


Figure 19b. CLOSE-UP OF NORMAL PLANE

By determining this gradient distance, the following general equation can be used to define the gradient's effect on the velocity.

$$V = V_7 + \frac{dV}{dy} y + \frac{dV}{dz} z \quad (11)$$

where  $y$  and  $z$  are the components of the gradient distance and  $dV/dy$  and  $dV/dz$  are indicators of the magnitude of the alpha and beta shear gradients respectively. To put this equation in a more usable form, the gradients are non-dimensionalized:

$$V = V_7 \left( 1 + \frac{s}{V_7} \frac{dV}{dy} \frac{y}{s} + \frac{s}{V_7} \frac{dV}{dz} \frac{z}{s} \right) \quad (12)$$

where  $s$  is the distance between the centers of opposite ports.

With this new equation, the terms  $\frac{s}{V_7} \frac{dV}{dy}$  and  $\frac{s}{V_7} \frac{dV}{dz}$  can be assigned a magnitude of relative gradient.

### C. Gradient Effects on Port Pressure Coefficients

For a uniform calibration the pressure at the peripheral holes may be found by the following expression.

$$C_{P_i} = C_{P_{i_c}} \left( 1 + \frac{s}{V_7} \frac{dV}{dy} \left( \frac{y}{s} \right) + \frac{s}{V_7} \frac{dV}{dz} \left( \frac{z}{s} \right) \right)^2 \quad (33)$$

Since  $C_{P_{i_c}}$  is a uniform coefficient based on the geometry of the slender body theory,  $V_i$  is the only term that accounts for gradient effects. Consequently,  $V_i$  in shear flow differs for each peripheral hole. If the velocity term is kept constant at  $V_7$  and the gradient effects are accounted for by the coefficients of pressure, the following expression results:

$$P_i = P_\infty + C_{P_{i_c}} \left( \frac{1}{2} \rho V_i^2 \right) \quad (34)$$

Solving Equations 33 and 34 for  $C_{P_i}$ , it is evident that pressure is proportional to the square of velocity in incompressible flow.

$$P_i = P_\infty + C_{P_i} \left( \frac{1}{2} \rho V_7^2 \right) \quad (35)$$

The relationship between the pressure coefficient and the gradient correction factor is given by the following expression.

Therefore, the pressure coefficient is a function of the velocity gradient.

$$C_{P_i} = C_{P_{i_c}} \left( \frac{V_i}{V_7} \right)^2$$

The relationship between the pressure coefficient and the velocity gradient is given by the following expression.

Therefore, the pressure coefficient is a function of the velocity gradient.

the determination of point (x,y,z). The vector analysis behind the location of point (x,y,z) is explained in detail in Johnson and Reed (Ref. 25). The results are as follows:

$$\begin{aligned}
 x &= x_1 + (x_7 - x_1) \cos\alpha \cos\beta - \cos\alpha \cos\beta [y_1 \sin\beta + z_1 \sin\alpha \cos\beta] \\
 y &= y_1 + (x - x_1) \tan\beta / \cos\alpha \\
 z &= z_1 + (x - x_1) \tan\alpha
 \end{aligned}
 \tag{37}$$

Port (i)	$x_1$	$y_1$	$z_1$
1	$s/2 \tan \epsilon$	$(s/2) \cos \theta_1$	$(s/2) \sin \theta_1$
2	$s/2 \tan \epsilon$	$(s/2) \cos \theta_2$	$(s/2) \sin \theta_2$
3	$s/2 \tan \epsilon$	$(s/2) \cos \theta_3$	$(s/2) \sin \theta_3$
4	$s/2 \tan \epsilon$	$(s/2) \cos \theta_4$	$(s/2) \sin \theta_4$
5	$s/2 \tan \epsilon$	$(s/2) \cos \theta_5$	$(s/2) \sin \theta_5$
6	$s/2 \tan \epsilon$	$(s/2) \cos \theta_6$	$(s/2) \sin \theta_6$
7	$d/2 \tan \epsilon$	0	0

Since  $x_1$ ,  $y_1$ ,  $z_1$ , and  $x_7$  are known values, the knowledge of alpha and beta will locate the point (x,y,z).

#### E. Shear Flow Measurement Corrections

At this point, the mathematical relationships necessary to compare the effects of velocity gradients are available. Equation 15 provides the ability to calculate  $C_\alpha$ ,  $C_{\alpha_c}$ , and  $C_\beta$ , and  $C_{\beta_c}$ , realizing that

$$\begin{aligned}
 C_{\alpha_1} &= \frac{P_4 - P_1}{P_7 - \bar{P}_{1-6}} = \frac{C_{p_4} - C_{p_1}}{C_{p_7} - C_{p_{1-6}}} & C_{\alpha_3} &= \frac{P_3 - P_5}{P_7 - P_{1-6}} = \frac{C_{p_3} - C_{p_5}}{C_{p_7} - C_{p_{1-6}}} \\
 C_{\alpha_2} &= \frac{P_3 - P_6}{P_7 - \bar{P}_{1-6}} = \frac{C_{p_3} - C_{p_6}}{C_{p_7} - C_{p_{1-6}}}
 \end{aligned}$$

By comparing the actual to the apparent angular pressure coefficients, the actual angles can be incremented until the apparent and actual coefficients are equal. This procedure indicates the flow angle errors inherent in the measurement of velocity gradients.

In order to determine the effects of different shear gradients at varying alphas and betas, Johnson and Reed (Ref. 25) calculated the apparent flow angles resulting from a span of actual flow angles and shear gradients. The calculations show the errors between the apparent angles and actual input values. Consequently, the actual flow angles can be determined by backstepping from the apparent angles. Although these calculations only allow manual corrections to apparent measurements, the theory of this section can be used to generate a family of data points. These points may then be input into a computer surface fitting scheme for highly accurate, near real-time correction to the apparent data.

#### 7. Seven-Hole Probe Measurement Capabilities

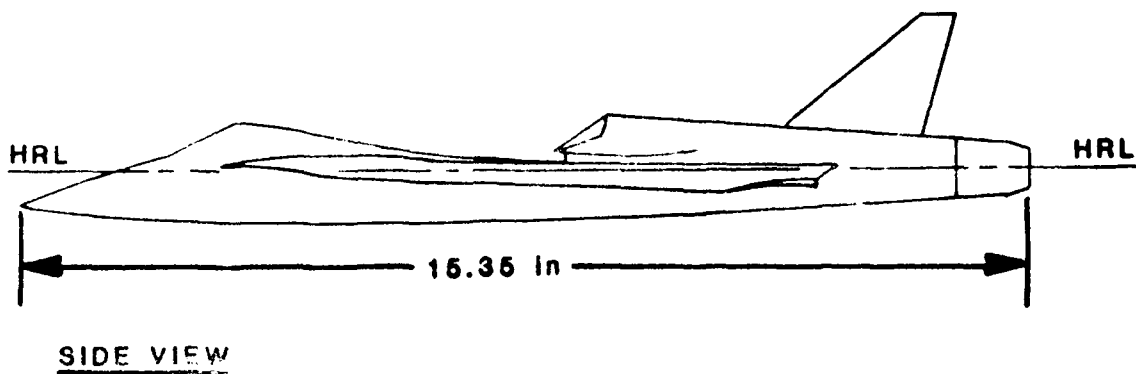
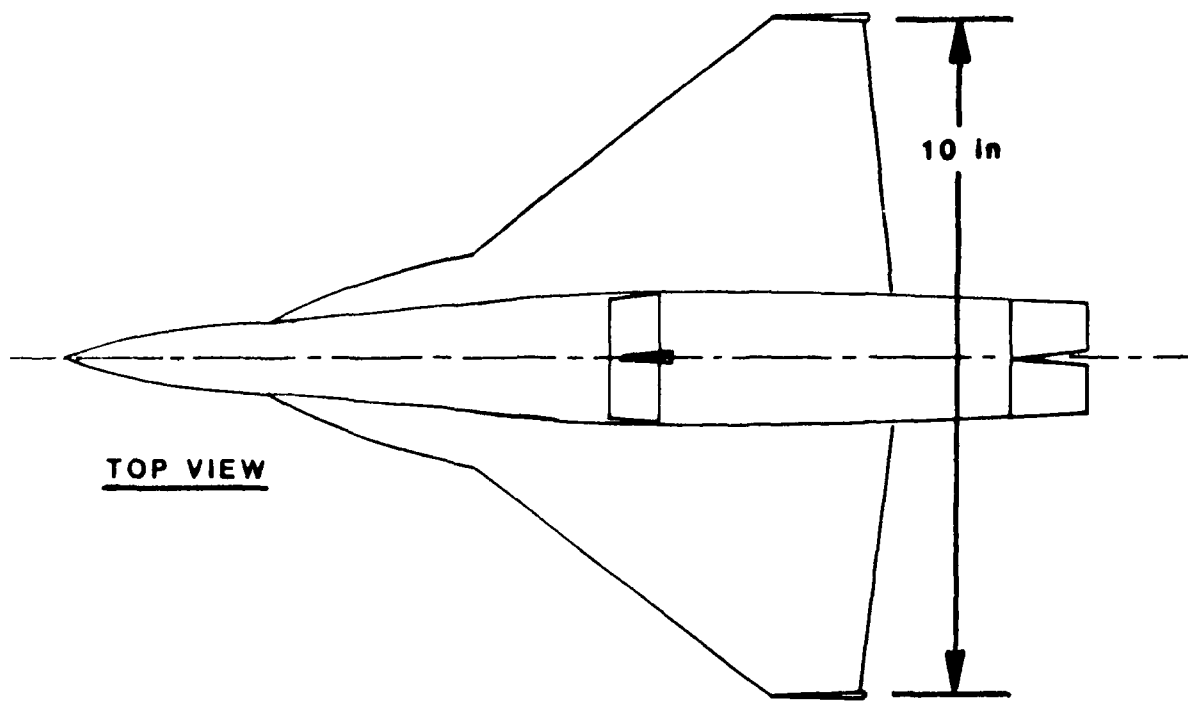
Three key elements of the seven-hole probe's measurement effectiveness in unknown flows are discussed further in order to provide an understanding of the basics behind its actual and potential capabilities. The three elements to be discussed are the probe's calibration, its installation, and its measurement error.

##### a. Calibration

The probe's calibration must be unique, calibrated due to manufacturing imperfections. The specifics of the seven-hole probe's calibration has been outlined in past sections. The probe's calibration is unique since the probe's calibration is

probes, seven-hole probe calibration allows for the relative flow angles, total pressure, and static pressure to be determined explicitly. With computer processing, these calculations are performed in near real time.

As discussed earlier, problems with the present calibration arise when attempting to make measurements in shear flow. This is because the present calibration and associated calibration coefficients are determined in a uniform flow. Jonas recorded measurement discrepancies in his attempts to use the seven-hole probe to map unknown flow fields with suspected shear (Ref. 26). Specifically, he compared seven-hole and total pressure probe measurements in a vortex wake created by the wing leading-edge extensions of a Northrop VATOL model.



1/40th Scale Northrop V-22 Concept

Figure 20. NORTHROP TOP-MOUNTED INLET V-22 CONCEPT

In a vertical flow, local total pressure should decrease through the wake because of viscous effects. This requires the coefficient (LOCAL  $\frac{P_{0L} - P_0}{P_0 - P_\infty}$ ) to be a negative value. The results of Jonas' pressure measurement comparison are shown in Table 1 below (Ref. 26).

Number of Readings (No. Data Samples for Readings)	Total Pressure Probe		
	Seven-Hole Pressure Probe (1)	Aligned with Freestream (2)	Aligned with Downwash (3)
Average Value	+0.197	-0.230	+0.160
Standard Deviation	+0.005	+0.007	+0.005
Maximum Value	--	-0.175	+0.140
Minimum Value	--	-0.067	+0.000
Number of Positive (Total Positive)	--	13	11

Jonas' calculations follow the discussion based on the results of Table 1 (Ref. 26). As can be seen from the data, the total pressure probe measurements do not agree with seven-hole probe measurements. For the total pressure probe aligned with the freestream flow, no measurements existed where  $\rho_{0L}$  was positive. However, these values may not be an accurate measure of local total pressure because flow angularity may have caused an expansion at the probe tip. For the total pressure probe aligned with the local flow, 76 percent of the measurements resulted in a local total pressure greater than that of the freestream value. These measurements, however, are lower than those obtained using

the seven-hole probe. One must realize that the total pressure probe was bent at an angle based on measurements made using the seven-hole pressure probe. Since the seven-hole measurements were made in a region of high shear flow, the local flow angularity reading may also be erroneous. Consequently, the flow around the tip of the total pressure probe supposedly aligned with the local flow might also be separated, again leading to false pressure readings. The average value for  $C_{TOTAL}$  of the bent total pressure probe, however, remains negative. This evidence seems to confirm our theoretical expectations of viscous effects.

Although the contradictory probe readings seem to indicate incorrect probe measurements in the high shear regime, the possibility of positive  $C_{TOTAL}$  regions may not be totally excluded. A vortex flow is very complex and not completely understood. Comparisons in a low shear flow environment (airfoil wake) of seven-hole probe measurements and hot-wire anemometer measurements are, however, very favorable and no discrepancies or positive  $C_{TOTAL}$  measurements exist (Ref. 26). This seems to indicate that the problem of positive  $C_{TOTAL}$ 's are only associated with high shear flows, and a major cause is the probe (manufacture, calibration, etc.) or the flow environment. The flow environment is not clearly defined, but it is likely that the probe is used in high shear flow environments.

#### Probe Construction

A pressure probe should be as small as possible to keep the flow disturbance to a minimum; however, it is accompanied by several other flow disadvantages. For example, smaller probes require more precise fabrication techniques. As size decreases,

tubes and other manufacturing imperfections cause greater probe construction errors, and the port tubes are more likely to break.

Although the five-hole probe may seem easier to construct than the seven-hole, the exact opposite is true. The construction of the seven-hole probe is greatly simplified since the port tubes are arranged in the only geometric fitting possible.

Hallington and Hollerbaugh (Ref. 27) explain that the difficulty with this geometric arrangement evaporates, and the probe is made easier to build in the five-hole probe.

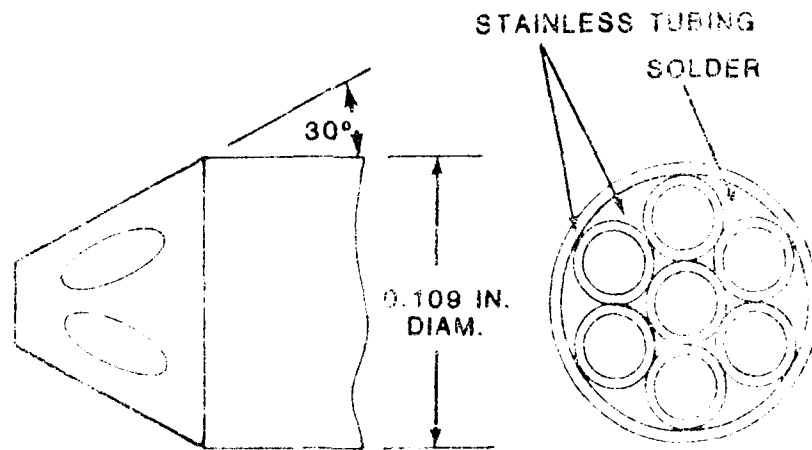


Figure 21. SEVEN-HOLE PROBE CONSTRUCTION

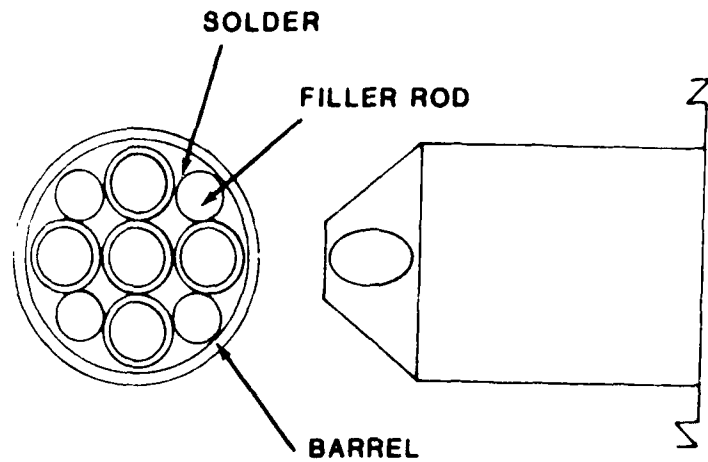


Figure 22. CONVENIENT PROBE DESIGN

First, it is difficult to hold five-hole tubing parallel with the center tube and in perfect azimuthal position for soldering.

Second, a high-powered magnifier is required to assure equal diameter on the four side tubes. Finally, there is no guarantee that the four solder fillets shown below will be equal or even nearly equal.

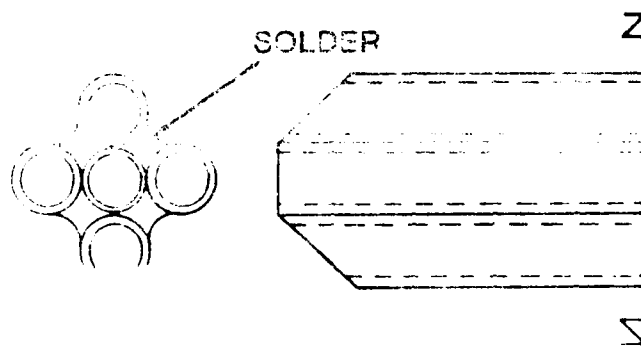
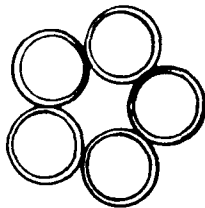


Figure 23. FIVE-HOLE PROBE ASSEMBLED FROM TUBES

As a quick note, a simpler geometric arrangement for five tubes is shown below. This order, however, lacks the required center tube.



**Figure 24. FIVE TUBES IN  
THE SMALLEST  
CIRCUMSCRIBED  
CIRCLE**

Over the years, multi-hole probe construction has uncovered certain features that increase the accuracy of pressure measurement. Total pressure measurement can be largely desensitized to alpha and beta by flaring the stagnation port at an angle of 30 to 60 degrees. Yet, the probe's overall sensitivity to flow angularity can be increased by decreasing the tip half-angle ( $\epsilon$ ). The drawback to a small half-angle is that the flow will separate from the leeward surface when  $\alpha_T$  exceeds  $\epsilon$  (Ref. 1).

#### C. Measurement Error Sources

Once smaller probes are built, they are more sensitive to measurement errors caused by flow debris and damage. These two effects can be minimized prior to use by reverse airflow through clogged ports, by dust covers over port entrances, and by simple,

careful handling of smaller probes.

Huffman identifies three other error sources that adversely affect a probe's measurement of pressure, orientation, and velocity (Ref. 1). These sources include the time lag between sensed and actual pressures, the pressure transducer resolution and frequency response, and the resolution of the analog-to-digital conversion. The pressure transducer resolution and analog-to-digital resolution are both beyond the scope of this report; however, the other error sources are discussed in the following paragraphs (Ref. 1).

As flow field conditions change, the probe surface pressures change nearly instantaneously. These pressure changes are transmitted to the pressure transducers by a finite amount of air through a connection tube. Huffman discusses the fact that the pressure lag caused by this finite travel time is related to the speed of pressure propagation and the pressure drop due to the viscous effects of the tubing (Ref. 1). Three physical characteristics directly affect this time lag:

1. Tubing diameter
2. Tubing length
3. Transducer cavity

The time lag is directly proportional to tubing length and inversely proportional to tubing diameter. The time lag increases with increasing tubing length. For a 1/8" ID transducer, a 1/4" tubing diameter results in a time lag of approximately 0.1 milliseconds. The time lag is directly proportional to the pressure pulse to propagate from the tubing exit to the transducer.

Benlapkohl and Buzzell (Ref 28) define frequency response as

the inverse of the maximum dwell time necessary for the probe system to react to the maximum pressure difference expected where the pressure sensed by the pressure transducer reaches 99 percent of the actual (surface) pressure.

Although pressure time lag is the major factor in the probe's frequency response, it is not the sole contributor. The frequency response of the transducer, the computational time required to convert the measured pressure to the desired output, the pressure differential between the probe tip and the transducer face, and the fluid density all affect the probe's overall frequency response (Ref. 28).

Probe frequency response rates are generally of a few Hertz. Because modern transducers and microprocessors require only milliseconds to operate, their operation is essentially instantaneous, and little can be accomplished in these areas to decrease the overall frequency response. The final two factors are associated with the fluid dynamic properties of the flow. The difference between the fluid pressure at a port entrance and the pressure at the transducer face acts as a driving potential, and a greater differential increases the frequency response (Ref. 28). Since a higher density increases the collision rate between molecules, and therefore, increases the propagation rate of a pressure pulse, greater density is synonymous with greater frequency response. In considering the effect of density, one must remember the assumption of a constant static pressure across the face of the probe. Remembering  $P = \rho RT$ , one should realize that the density of the flow is dependent upon pressure.

### 3.2.2.2 Measurements of Unknown Flows

The test was conducted with the seven-hole probe center on two vortex lines to determine the capabilities and limitations of the probe in the presence of unknown flow fields. The following test objectives were set. These two objectives are accomplished in the vortex flow field vortex flow:

1. In the presence of a vortex flow, a finite wing section of a NACA 0008 airfoil was placed in the two by three foot subsonic wind tunnel at the United States Air Force Academy (Figure 25). The test was run with the wing at an angle of attack of 8 degrees and a uniform flow velocity of 150 ft/sec.

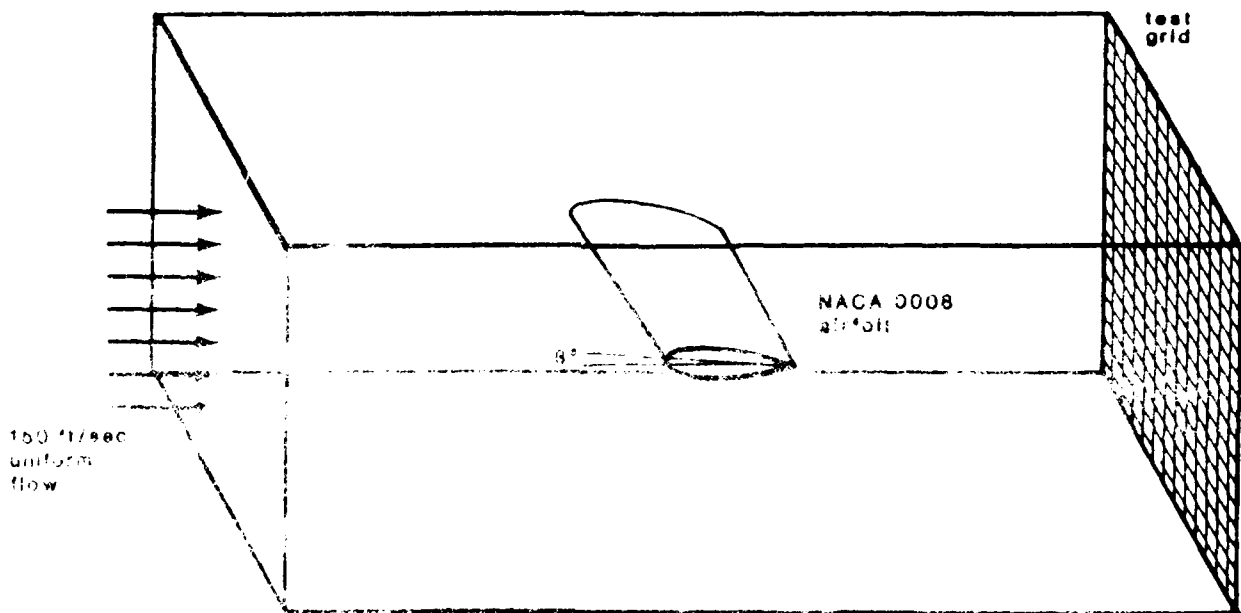


Figure 25 WING VORTEX TEST

Computer graphing techniques were used to map out the flow velocities and directions for all the points in a series of parallel two-dimensional planes, all of which were perpendicular to the uniform flow.

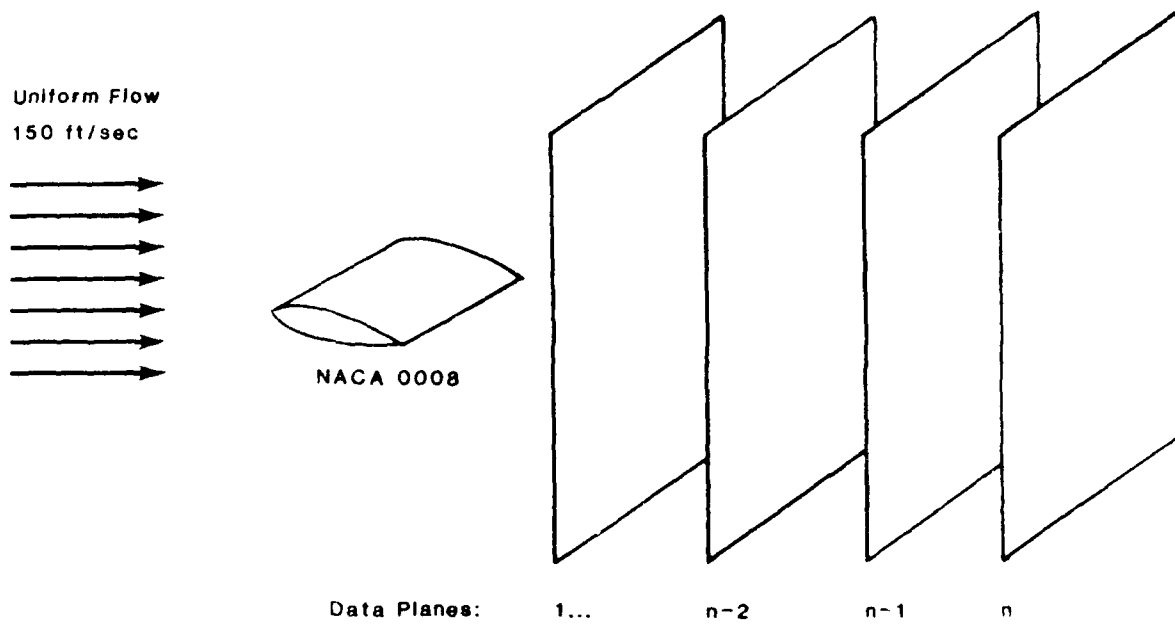


Figure 26. WING VORTEX DATA PLANES

The two-dimensional planes or test grids, started twelve inches aft of the wing's trailing edge and moved forward (toward the wing) by two inch increments for every data set. From these test runs, capabilities and limitations of the seven-hole probe under mild gradient conditions are examined and a wingtip vortex is mapped.

#### a. Crossflow Velocities

The first step in vortex analysis is to examine the crossflow velocities in each plane. Crossflow velocity plots, which are scaled by a factor of two are shown in Figures 27a to 27h ( Ref. 29). With past errors in gradient regime, one would expect errors in seven-hole readings. Suspect data of this nature (Ref. 29) are identified by inconsistencies in the crossflow plots, such as an inordinately large or small arrow (Fig. 28) or an arrow in the wrong direction. However, the actual crossflow plots do not confirm these expectations. The velocities are well-behaved, and no inconsistencies are seen near the vortex core where high shear exists.

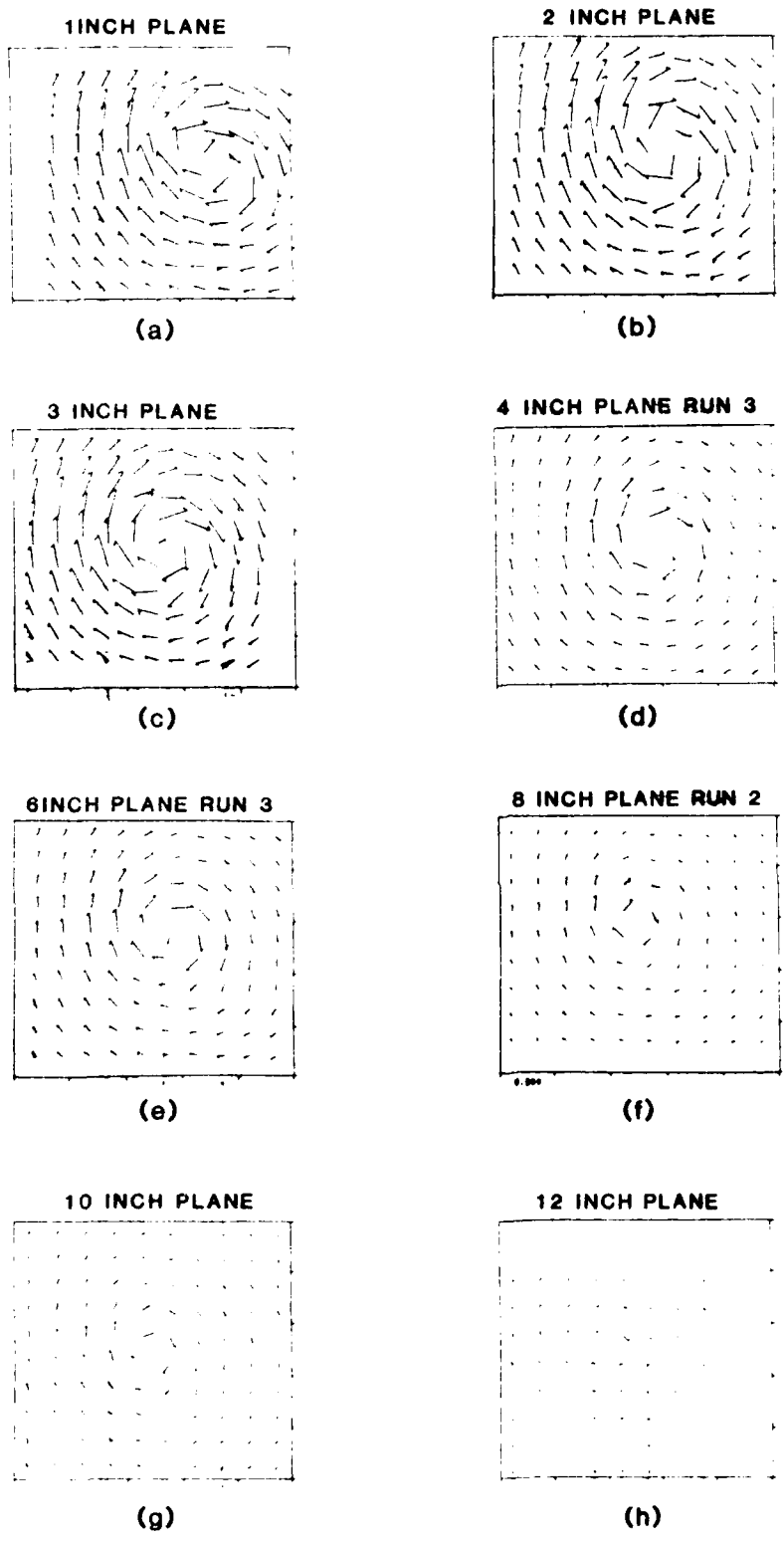


Figure 27. CROSSFLOW VELOCITIES OF WING TIP VORE VORTEX

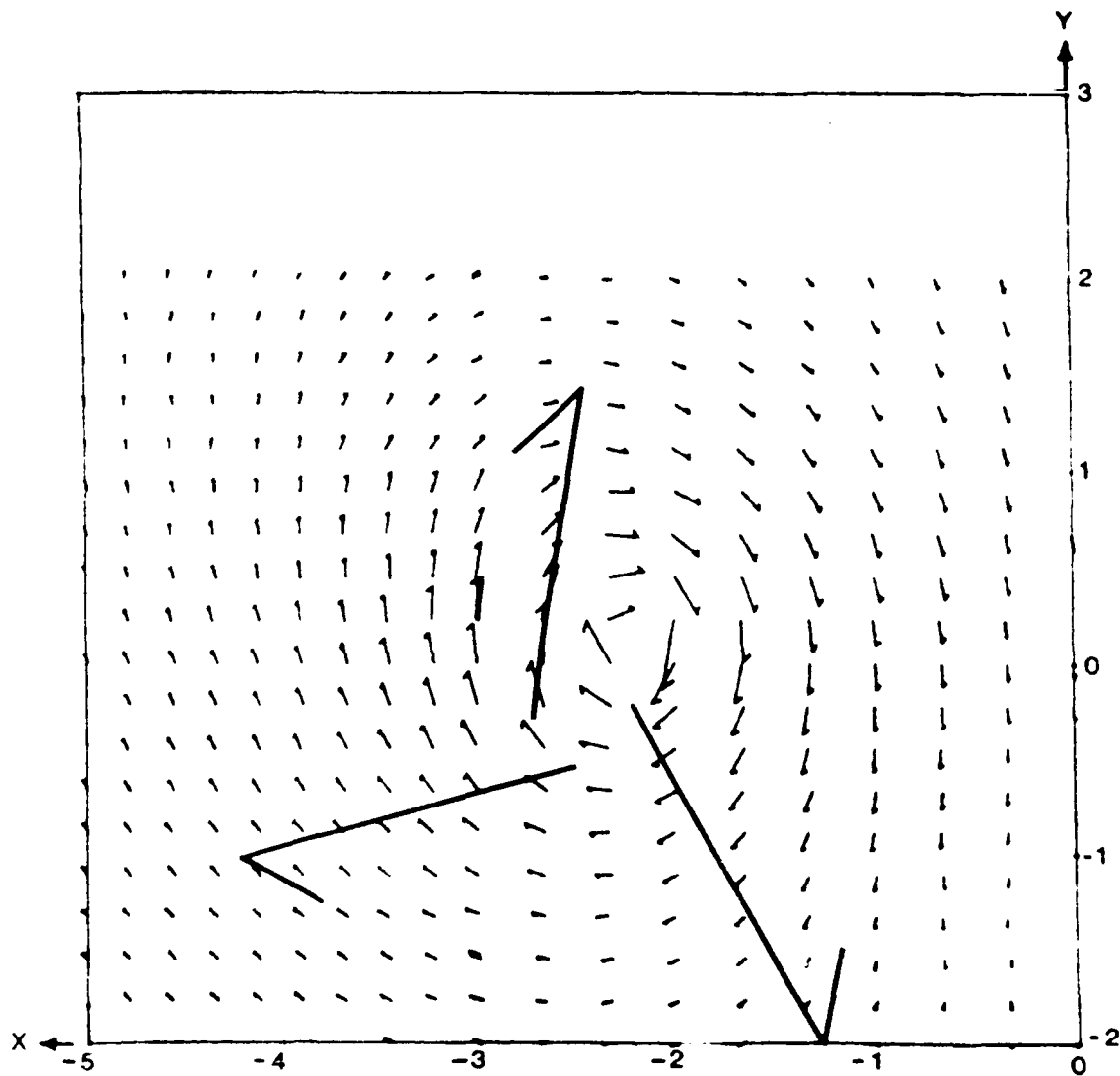


Figure 28. CROSSFLOW DATA ERRORS

Complete sets of velocity data may be shown on a velocity magnitude centerline plot for ease of analysis (Figure 29).

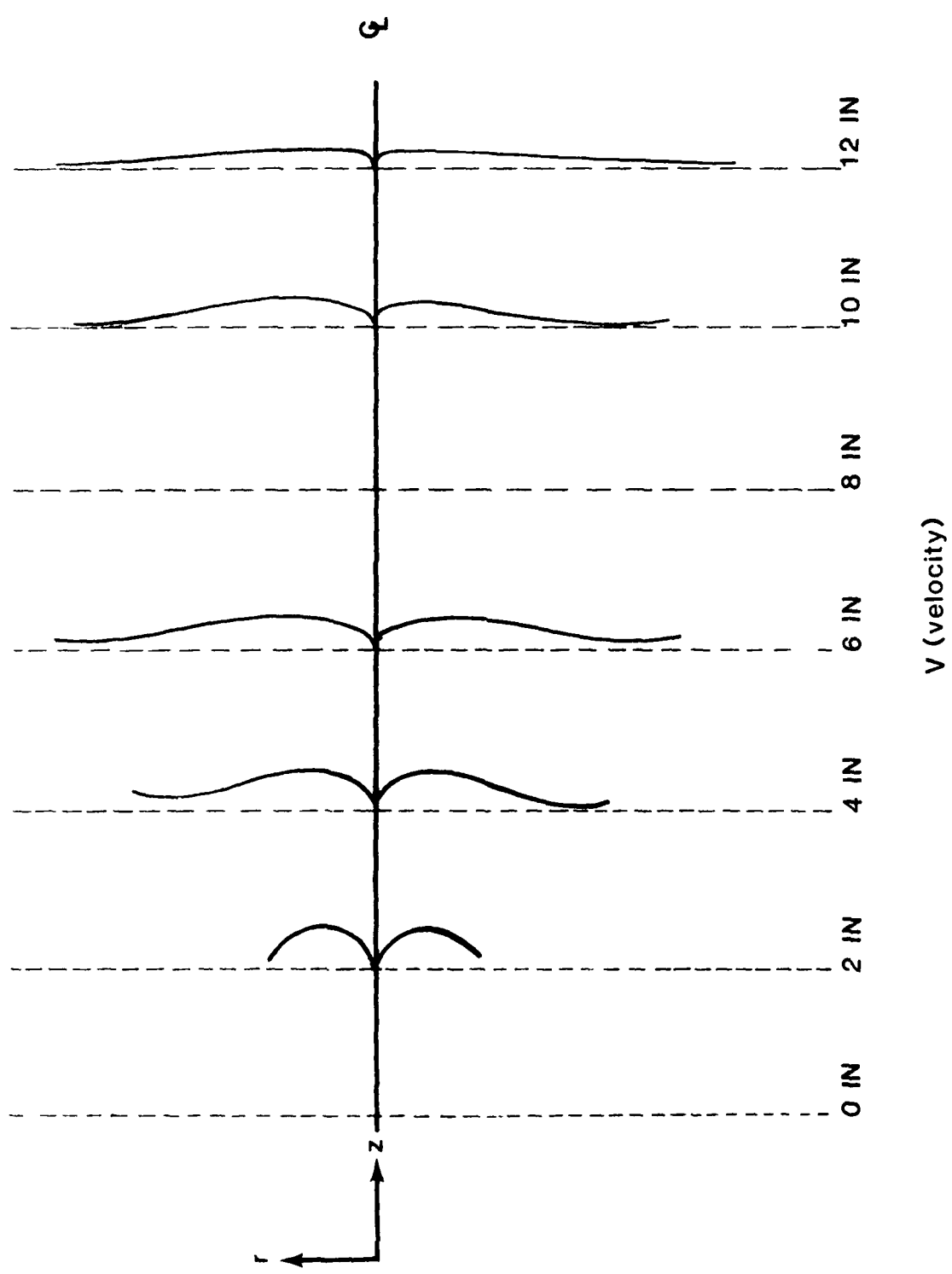


Figure 29. MAGNITUDE OF CROSSFLOW VELOCITY

This new representation of the velocity data shows how the vortex expands and decays as it moves downstream. Represented by the velocity magnitude, the vortex strength decreases as the vortex expands. The vortex velocity gradient also decreases since the vortex is diffusing. Discontinuities do occur, however, at the eight-inch plane. As seen in Figure 29, the velocity magnitudes are smaller than those for the six-inch plane, but they are also smaller than those in the ten-inch plane. This data must be incorrect, for the vortex cannot be weaker at eight inches downstream than it is at ten inches. Because of the suspect data, the eight-inch plane is removed from future analysis.

In order to find a point at which the velocity gradient in the flow is great enough to induce noticeable error, additional measurements were taken at planes one-quarter and one-half inch behind the trailing edge. Again, the seven-hole probe exceeds expectations by revealing no such noticeable error. The crossflow plots for the two additional planes are shown in Figures 30a and 30b and are scaled by a factor of ten.

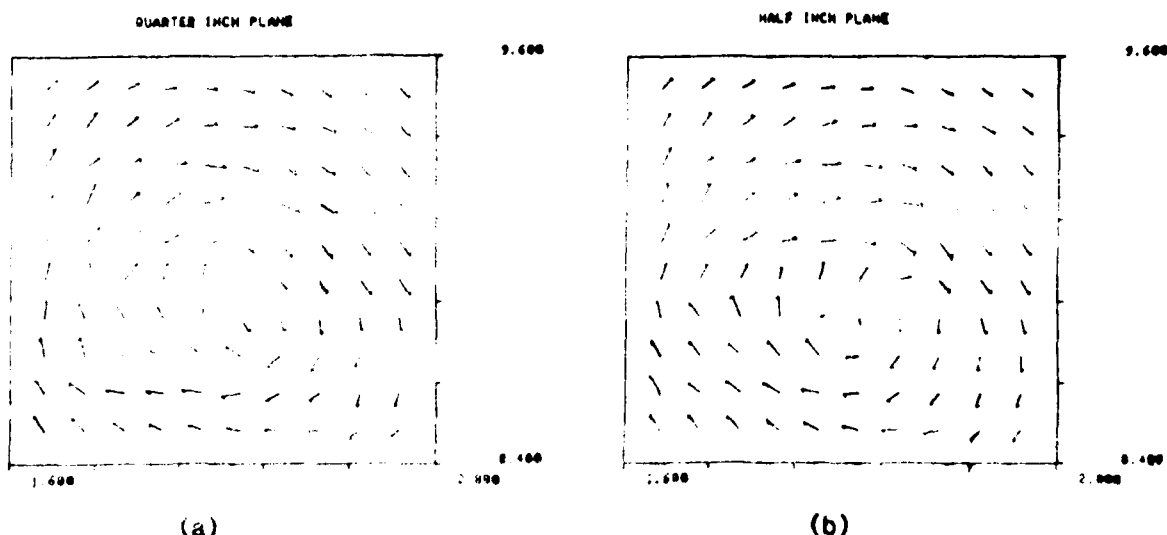


Figure 30. CROSSFLOW VELOCITY OF WING TIP VORTEX

### C. Definition of Flow Field Pressure Coefficients

Because pressure measurements are affected by slight shifts in wind tunnel velocity and temperature, pressure coefficients are used when the local and total tunnel pressures are compared and non-dimensionalized by the tunnel dynamic pressure. These three coefficients are defined below:

$$\begin{aligned} C_{\text{STATIC}} &= \frac{P_{\infty L} - P_{\infty}}{P_0 - P_{\infty}} \\ C_{\text{TOTAL}} &= \frac{P_{0L} - P_0}{P_0 - P_{\infty}} \\ C_{\text{DYN}} &= C_{\text{TOTAL}} - C_{\text{STATIC}} = \frac{P_{0L} - P_{\infty L}}{P_0 - P_{\infty}} - 1 \end{aligned} \quad (39)$$

Probe measurement errors may be found by determining the correct values for these three pressure coefficients, either theoretically or experimentally with another device, and comparing these values with actual seven-hole probe data. Vortex pressure coefficient trends may be found through analysis of a two-dimensional vortex.

### D. $C_{\text{TOTAL}}$

For an ideal two-dimensional vortex, angular velocity increases inversely as the distance to the vortex center decreases (Figure 31). Real vortices, however, are subject to viscous effects. Outside of point A, the flow is essentially inviscid. Inside that point, viscous forces reduce angular velocity until it reaches zero at the vortex center.

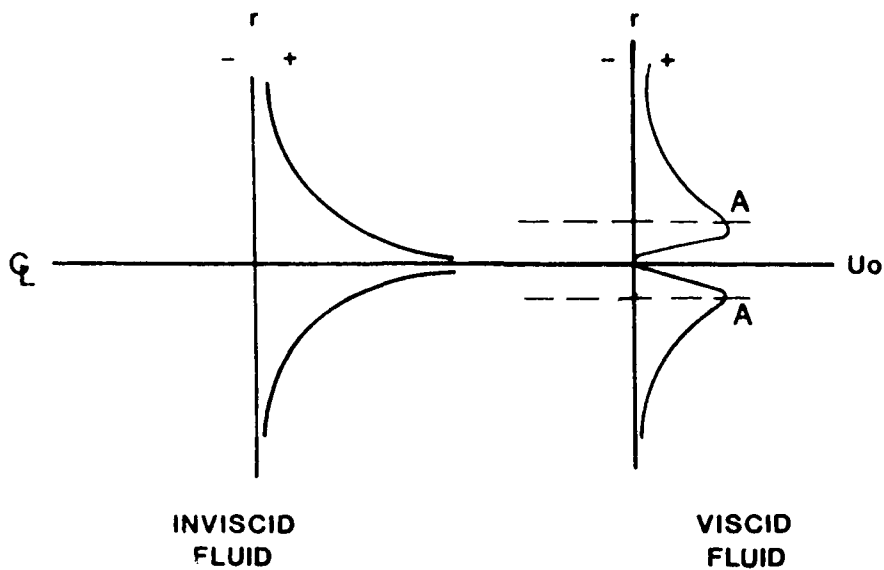
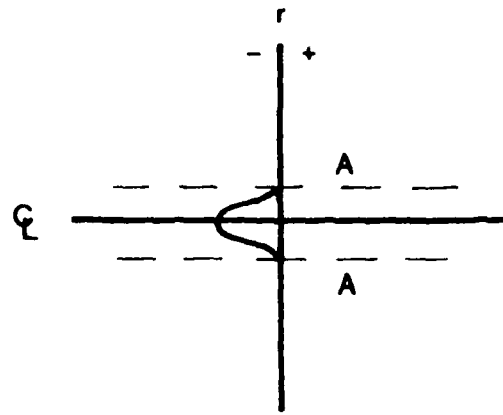


Figure 31. ANGULAR VELOCITY OF VORTEX

These two flow regions directly affect  $C_{TOTAL}$  values. Because total pressure is constant in incompressible, inviscid flow,  $C_{TOTAL}$  is zero in the inviscid region. On the other hand, the viscous forces found within the vortex core decrease the flow's fluid-mechanical energy.  $P_0$  decreases causing  $C_{TOTAL}$  to become lower. Figure 31 diagrams  $C_{TOTAL}$ 's expected behavior.



$C_{TOTAL}$

Figure 32. VORTEX  $C_{TOTAL}$

The expected shape was derived by Jonas (Ref. 26) from theoretical considerations of a 2-D vortex decaying with time (Equation 40).

$$\frac{p_{oL}}{r} = \frac{r}{r} \left( \frac{r_1}{2\pi} \right)^2 \frac{1}{2vt} e^{-r^2/4vt} (1 - e^{-r^2/4vt}) \quad (40)$$

As discussed, the bucket-shape phenomenon is present in the experimental vortex data shown in Figure 33.

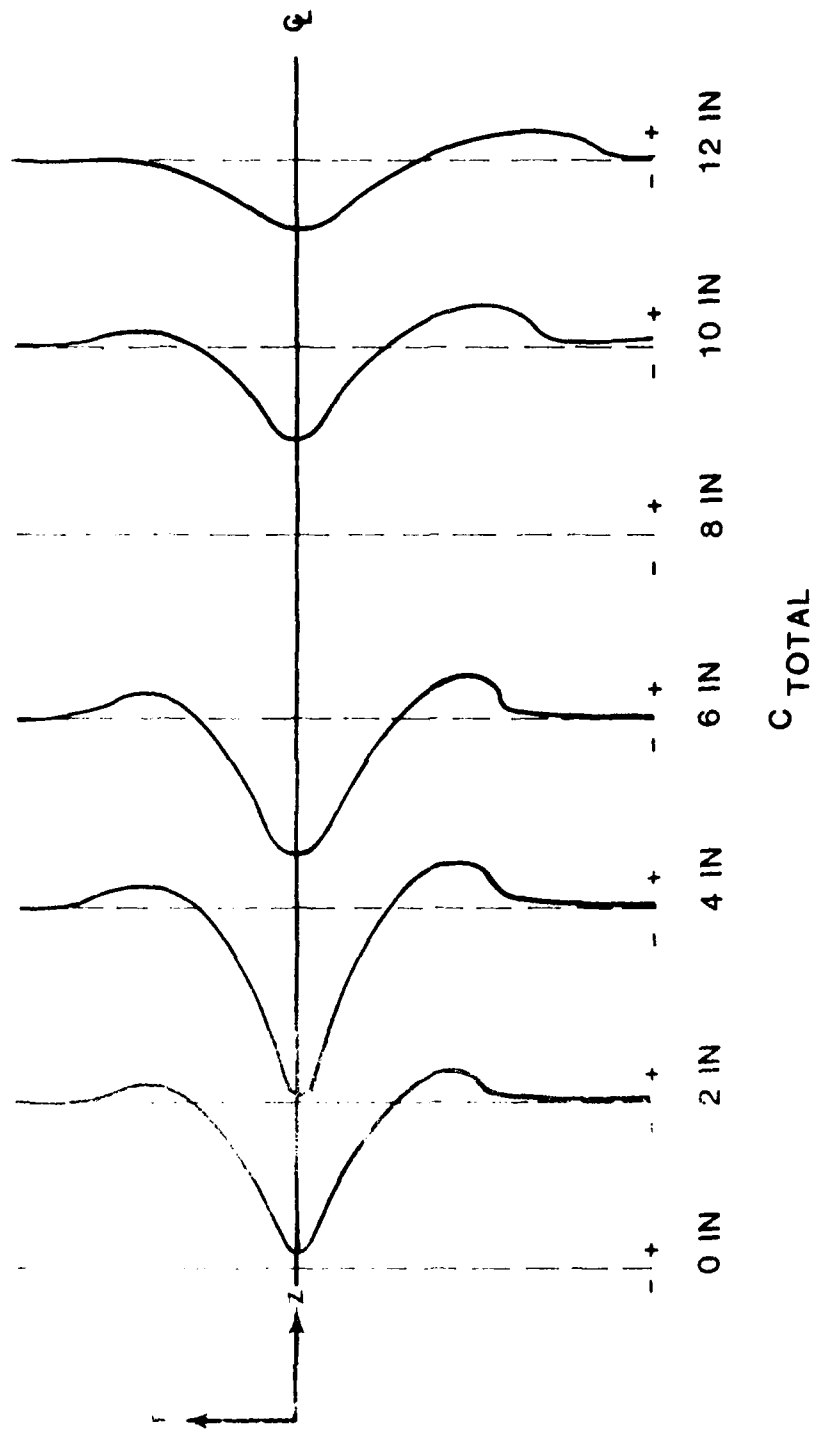


Figure 33.  $C_{TOTAL}$  OF WING VORTEX

As the flow progresses downstream, lower velocity gradients produce smaller viscous forces, smaller deficits of fluid-mechanical energy, and small bucket-shaped area plots. The two areas of positive  $C_{TOTAL}$  in each of the centerline plots is unexpected. The fact that the magnitude of the positive  $C_{TOTAL}$  values is always greater on the outboard side of the wing than on the inboard side is inexplicable. The sets of contour plots and axonometric plots (Appendix A) show that  $C_{TOTAL}$  is positive only on the two sides of the vortex parallel to the wing. The vortex data behaved normally above and below the wing. In duplicating Jonas's previous positive  $C_{TOTAL}$  results the vortex data seem to indicate a limitation in the seven-hole probe's measurement capabilities. It is still possible, however, that the positive  $C_{TOTAL}$  values may be the result of a transfer mechanism that is not yet understood.

#### E. $C_{STATIC}$

Like  $C_{TOTAL}$ , the presence or absence of viscosity affects the values of  $C_{STATIC}$ . At freestream conditions,  $C_{STATIC}$  equals zero. Progressing inward from the freestream conditions to point A, the angular velocity increases, static pressure drops, and  $C_{STATIC}$  decreases from zero to a negative value. To determine what happens in the viscous region, the following mathematical analysis is required.

$$\frac{dp}{dr} = \frac{\rho u^2}{r}$$

For a free vortex  $u = \frac{c}{r}$  so,  $\frac{dp}{dr} = \frac{\rho c^2}{r^3}$

For solid body rotation  $u_0 = \omega r$  so,  $\frac{dp}{dr} = \rho \omega^2 r$

Integrating for  $p$  results in the following:

$$P = C_1 - \frac{\rho C^2}{2r^2} \quad (41a)$$

$$P = C_2 + \frac{\rho \omega^2 r^2}{2} \quad (41b)$$

Equations 41a and 41b when superimposed reveal a bucket-shape like form of  $C_{TOTAL}$ . The entire  $C_{STATIC}$  curve is shown in Figure 34.

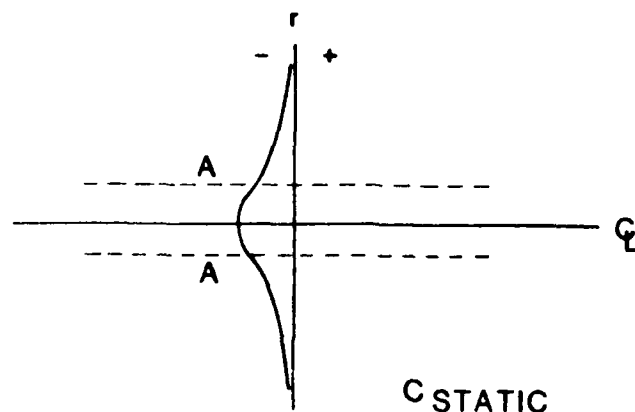


Figure 34. VORTEX  $C_{STATIC}$

#### B. $C_{DYNAMIC}$

$C_{DYNAMIC}$  is simply the subtraction of  $C_{STATIC}$  from  $C_{TOTAL}$  as shown in equation 39. Again, at the freestream,  $C_{DYNAMIC}$  is identically zero.  $C_{DYNAMIC}$  equals the absolute value of  $C_{STATIC}$  from the freestream conditions inward to point A since  $C_{TOTAL}$  is zero. At the center of the vortex, local velocity and therefore local dynamic pressure are zero causing  $C_{DYNAMIC}$  to equal -1. From point A to the center,  $C_{DYNAMIC}$  changes as in Figure 35.

Insert Figure 35

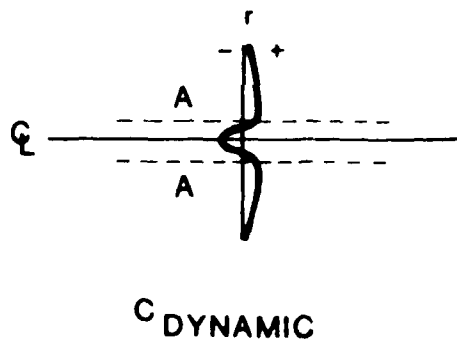
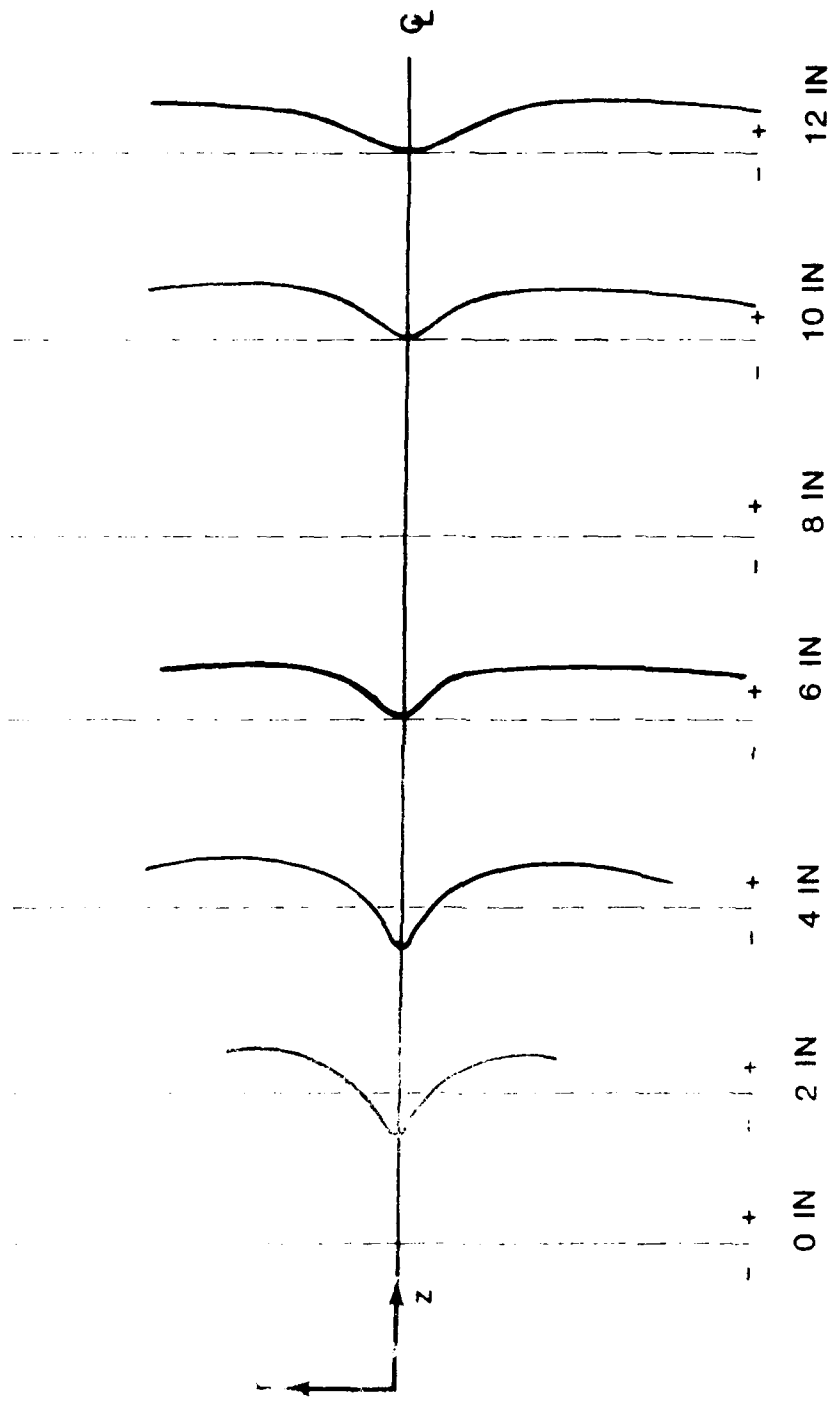


Figure 35. VORTEX  $C_{DYNAMIC}$

Experimental data supports the theoretical analysis of  $C_{DYNAMIC}$ .



C DYNAMIC

Figure 36. C DYNAMIC OF WING VORTEX

This seems somewhat surprising in lieu of the questionable positive  $C_{TOTAL}$  values. The important factor missing from the coefficient plots are the relative magnitudes. Because  $C_{TOTAL}$  values are very close to zero, the contribution of  $C_{TOTAL}$  is not very significant in the calculation of  $C_{DYNAMIC}$ .

#### I. Research Applications

Today's flow mapping efforts are much more complex than the vortex example. Besides Jonas' VATOL flow field measurements, seven-hole probe work at the Air Force Academy has examined canard wakes, lifting surface wakes of canard/swept wing aircraft, and flow field characteristics of square cross-sectional missile bodies. Probe calibration and measurement of unknown flowfields have also been conducted at the NASA Ames Research Center in the 8x7 foot and 14 foot transonic wind tunnels (Ref. 30).

Measurements of wing and canard jet-flap effects as well as the effects of prop fan installations have been made with multiple and single probe installations. Yet, these more complex research efforts are founded on the basic analysis and data presentation explained in the vortex example.

Griffin (Ref. 31) used cross velocity and pressure contours in his study of canard/forward swept wing aircraft. Figures 37 and 38 show the two types of data plots in the same spatial relationship that their data points have to the model.



Figure 37. TYPICAL VELOCITY DATA  
PLANE LOCATION  
RELATIVE TO MODEL

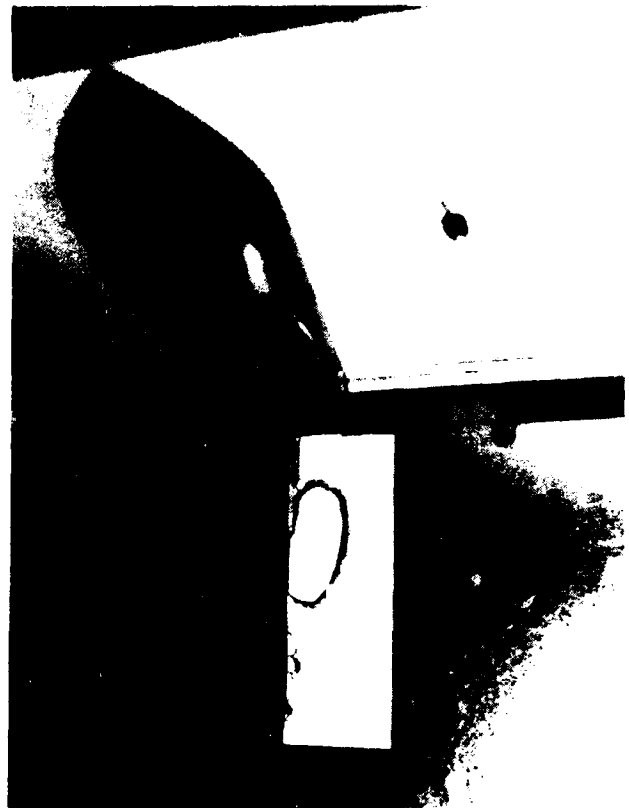


Figure 38. TYPICAL PRESSURE DATA  
PLANE LOCATION  
RELATIVE TO MODEL

Jonas (Ref 26) superimposed these two types of plots in his investigation of  $C_{TOTAL}$  (see Figure 39).

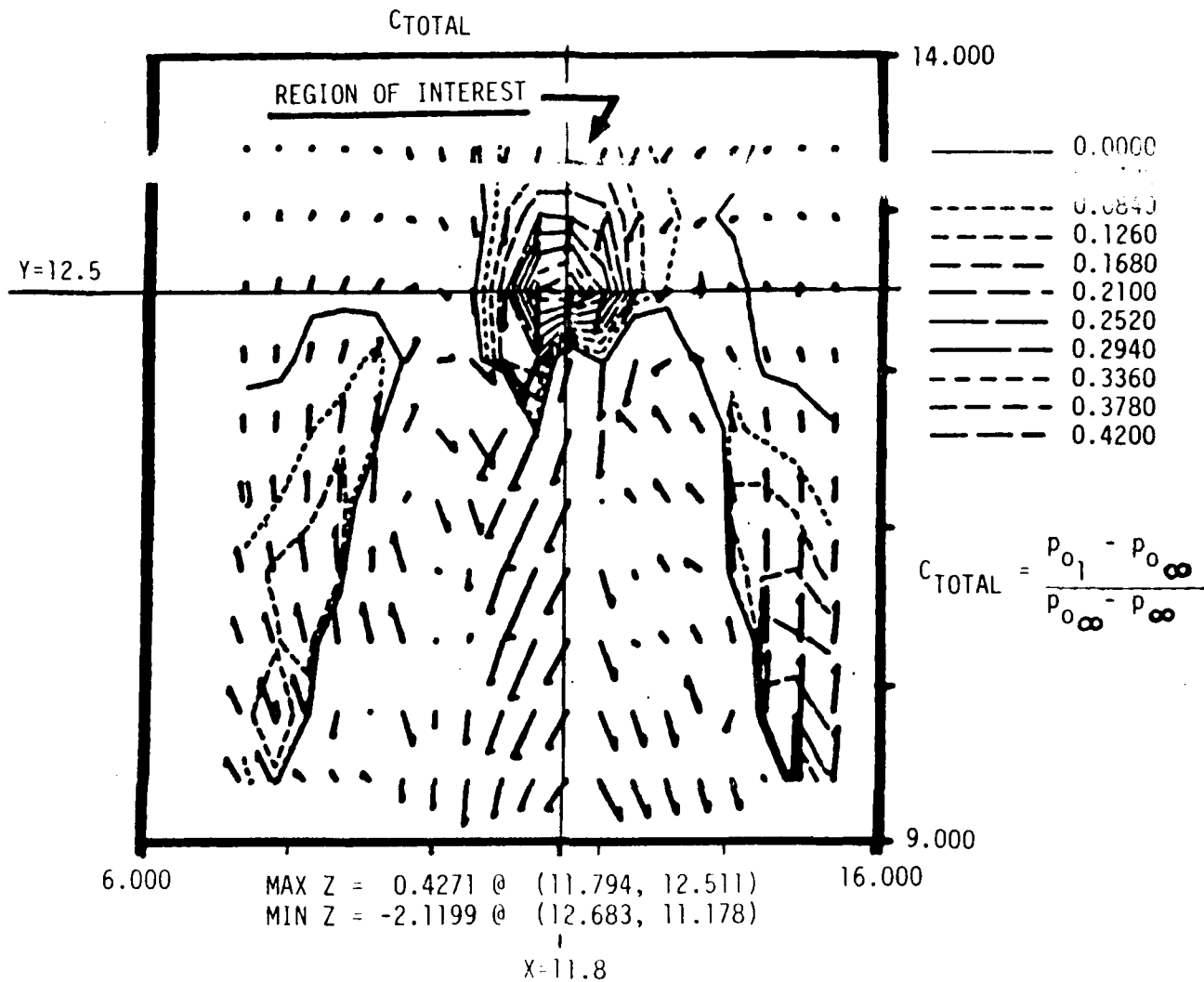
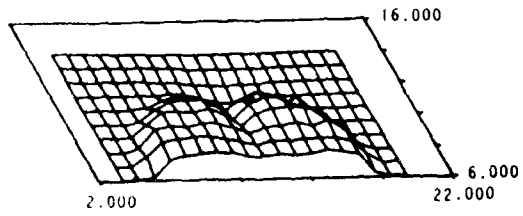


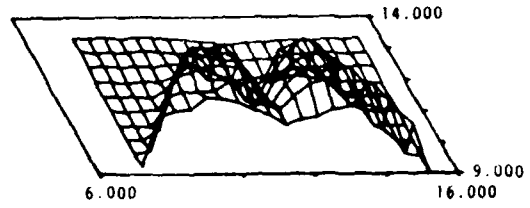
Figure 39. REGIONS OF POSITIVE  $C_{TOTAL}$ , DATA PLANE ZMP75

Jonas also used a series of axonometric projections to analyze the growth (diffusion) and decay (dissipation) of vortices. Evidence of mixing is found in the relative flattening of the  $C_{TOTAL}$  values (negative  $C_{TOTAL}$  being up or out of the plane of projection).

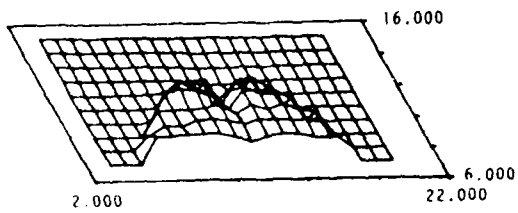
NASA MODEL, STRUT MOUNT, ZP6 15:27 16-SEP-82  
CTOTAL



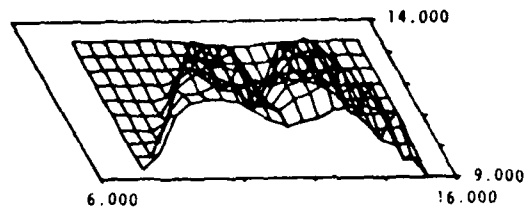
NASA MODEL, STRUT MOUNT, Z0  
CTOTAL



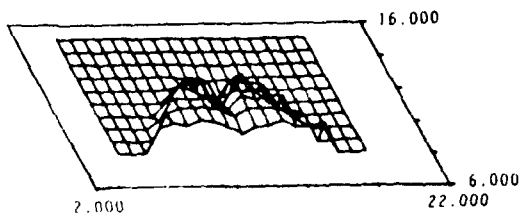
NASA MODEL, STRUT MOUNT, ZP2 14:46 16-SEP-82  
CTOTAL



NASA MODEL, STRUT MOUNT, ZMP25  
CTOTAL



NASA MODEL, STRUT MOUNT, ZP1 12:15 16-SEP-82  
CTOTAL



NASA MODEL, STRUT MOUNT, ZMP5 19:53 14-SEP-82  
CTOTAL

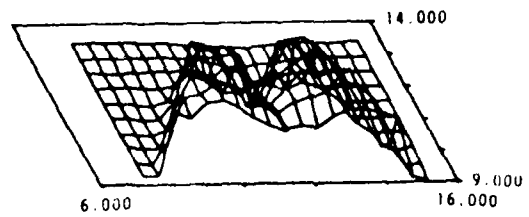


Figure40. AXONOMETRIC PROJECTIONS, C TOTAL, DATA PLANES ZP6 TO ZMP5

Gerner and Durston at NASA Ames took Jonas' data and produced a series of 12 color contour photographs that span the development through decay of the VATOL vortices. The study was limited to the examination of local total pressure or  $C_{TOTAL}$ . The color contours allow more detail in data representations by making pressure differences easier to see. Regions of positive  $C_{TOTAL}$  are clearly distinguished from other points in the flow field. As seen in the other data schemes, the color contours reveal that the VATOL is in a slight sideslip. This causes the right vortex to burst prior to the left vortex.

#### VII. Conclusions

As shown, the seven-hole pressure probe remains a valuable measurement tool for the documentation of unknown flowfields. The device has a greater measurement range and flexibility than other similar obtrusive flow measuring devices. The seven-hole probes themselves are easily constructed and calibrated for use in subsonic compressible flows. Measurements in adverse shear flows can be corrected to give actual flow conditions based on the methodology developed in this paper. Finally, as shown in the application section, the probe is not only a valuable research device but educational as well in demonstrating fundamental flow properties.

#### VIII. Acknowledgement

The authors would like to acknowledge Lt. Col. Roger Gallington, who developed the methodology for the seven-hole pressure probe. The authors would also like to thank Mr. Don Durston of the NASA Ames Research Center and the faculty and cadets of the USAF Academy who aided in the completion of this effort.

## Symbols

$A_i$	the $i$ th value of a particular data point either known or determined from calibration equations
$C_{DN}$	local dynamic pressure coefficient
$C_{APM}$	coefficient representative of compressibility effects
$C_D$	apparent total pressure coefficient
$C_p$	coefficient of pressure
$C_{D1}$	apparent dynamic pressure coefficient
$C_{DSTATIC}$	local static pressure coefficient
$C_{DTOTAL}$	local total pressure coefficient
$\alpha$	angle of attack pressure coefficient
$\beta$	angle of sideslip pressure coefficient
$C_{\beta}$	roll angle pressure coefficient
$C_{\alpha}$	pitch angle pressure coefficient
$f$	body geometry function
$K_i$	calibration coefficients
$l$	length
$M$	Mach number
$P$	pressure
$q$	dynamic pressure
$(r, \theta, z)$	cylindrical coordinates
$R$	radius
$s$	distance between centers of opposing holes
$u$	local velocity, perturbation velocity component
$V$	velocity
$(x, y, z)$	Cartesian coordinates
$\alpha$	angle of attack
$\beta$	angle of sideslip

$\delta$   $\sqrt{1-M_\infty^2}$   
 $\epsilon$  probe tip half angle  
 $\xi$  ratio of specific heats  
 $\psi$  roll angle  
 $\rho$  density  
 $\nu$  pitch angle

subscripts

$C$  uniform incompressible flow  
 $(i, j)$  local property or condition  
 $o$  total or stagnation condition  
 freestream conditions

References

1. Huffman, G.J.D., Theory, Performance and Design of Flow Direction and Mach Number Probes, AFATL TR-81-44, Air Force Armament Laboratory, Eglin AFB, Florida, April 1981.
2. Gerner, A.A. and C.L. Mauer, "Calibration of Seven-Hole Probes Suitable for High Angles in Subsonic Compressible Flows," Aeronautics Digest, USAFA-TR-81-4, USAF Academy, Co., May 1981.
3. Schultz, W.M. et.al., "Several Combination Probes for Surveying Static and Total Pressure and Flow Direction, NACA TN 2830, 1952.
4. Kettle, D.J., "Design and Calibration at Low Speeds of a Static Tube and Pitot-Static Tube with Semi-Ellipsoidal Nose Shapes," J. Roy. Aero. Soc., Vol. 58, p. 835, 1954.
5. Smetena, F.O. and J.W.M. Stuart, A Study of Angle-of-Attacks Angle-of-Sideslop Pitot-Static-Probes, WADC TR 5723A, AD 118209, 1957.
6. Bryer, O.W. et.al., "Pressure Probes Selected for

- Three-Dimensional Flow Measurement," Rep.Mem. Aero Res. Coun.  
London, No. 3037, 1958.
7. Morrison, E.F. et.al., "Hole Size Effect on Hemisphere Pressure  
Distributions." J.Roy. Aer. Soc., Vol. 71, 1967.
8. Wright, M.A., "The Evaluation of a Simplified Form of  
Representation for Spherical and Hemispherical Pitometer Calibration  
Data," J. Sci. Instr. (J. Phys. E). Vol. 3, p. 456, 1970.
9. Donald, V.W. et.al., An Investigation of the Three-Dimensional  
Flow Characteristics of a Non-Nulling Five-Tube Probe, Nat. Res.  
Council of Canada, Aero Rpt. LR-393, NRC No. 7964, 1964.
10. Dudzinski, J.T. and L.N. Krause, Flow Direction Measurement  
with Fixed-Position Probes, NASA TMX-1904, 1969.
11. Beecham, L.J. and S.J. Collins, Static and Dynamic Response of  
a Design of a Differential Pressure Yawmeter at Supersonic Speeds,  
Roy. Aer. Est. Report No. GW 19, 1954.
12. Hutton, P.G., Static Response of a Hemispherical-Headed  
Yawmeter at High Subsonic and Transonic Speeds, Roy. Aero. Est.  
Tech. Note N. Aero 7525, CP No. 401, 1957.
13. Nowack, C.F.R., "Improved Calibration Method for a Five-Hole  
Spherical Pitot Probe," J. Sci. Instr. (J. Phys. E.), Vol. 3,  
p. 41, 1970.
14. Lee, H., et.al., "The Probes for the Measurement of the  
Complete Velocity Vector in Subsonic Flow," Aero. J., Vol. 72, p.  
1000, 1968.
15. Spaid, F.W. et.al., "Minature Probe for Transonic Flow  
Direction Measurement," AIAA J., Vol. 13, p. 253, 1975.
16. Glawe, G., et.al., A Small Combination Sensing Probe for  
Measurement of Temperature, Pressure and Flow Direction; NASA TN

D-4816, 1968.

17. Treaster, A.L. and A.M. Yocum, "The Calibration and Application of Five-Hole Probes," Penn. State Univ. Applied Research Laboratory Report TM 78-W, 1978.

18. Bryer, D.W. and D. W. Pankhurst, "Pressure Probe Methods for Determining Wind Speed and Flow Direction," Published by Her Majesty's Stationery Office, London, England, 1971.

19. Wuest, W., "Measurement of Flow Speed and Flow Direction by Aerodynamic Probes and Vanes," Paper Presented at the 30th Flight Mechanics Panel Meeting in Montreal, Canada, 1967.

20. Huffman, G. David, "Flow Field Characteristics of Flow Direction and Mach Number Probes Using Slender Body Theory," Aeronautics Digest, USAFA-TR-79 1, USAF Academy, CO, Feb. 1979.

21. Hess, J.L. and A.M.O. Smith, "Calculation of Potential Flow about Arbitrary Bodies," Progress in Aeronautical Sciences, Vol. 8, Pergamon Press, p.81, 1966.

22. Smith, A.M.O. and A.B. Bauer, "Static-Pressure Probes that are Theoretically Insensitive to Pitch, Yaw and Mach Number," J.Fl. Mech., Vol.44 p. 513, 1970.

23. Liepmann, H.W. and A. Roshko, "Elements of Gas Dynamics," John Wiley and Sons, New York, 1958.

24. Gallington R.W. "Measurement of Very Large Flow Angles with Non-Nulling Seven-Hole Probes," Aeronautics Digest, USAFA-TR-80-17, USAF Academy, Co., October 1980.

25. Reed, L.S. and G.H. Johnson, "Seven-Hole Probe in Shear Flow," AIAA Paper 85-0076 (to be published).

APPENDIX A

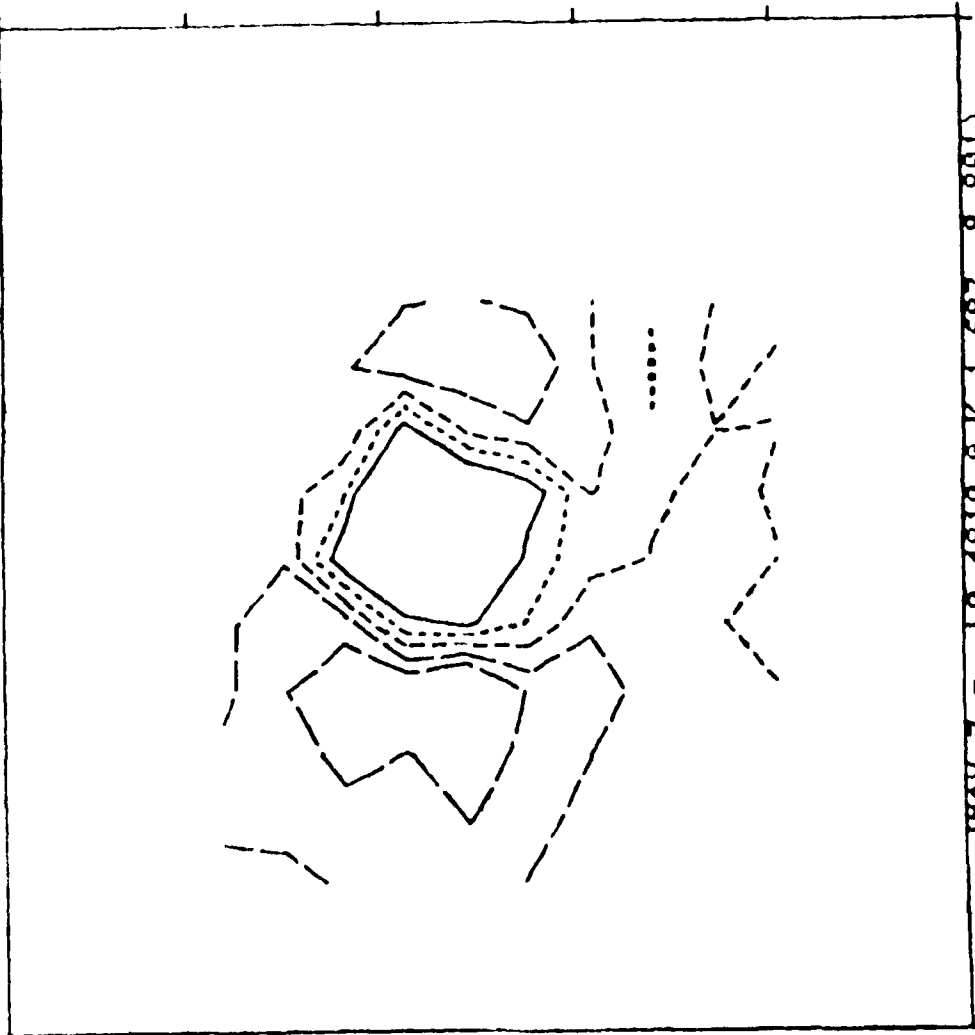
Wing Tip Vortex CTOTAL Plots

2 INCH PLANE

CTOTAL

10.500

-0.2000  
-0.1000  
0.0000  
0.1000  
0.2000



7.000

4.000

0.500 MAX Z = -8:4918 0 { 2:583; 9:823 }

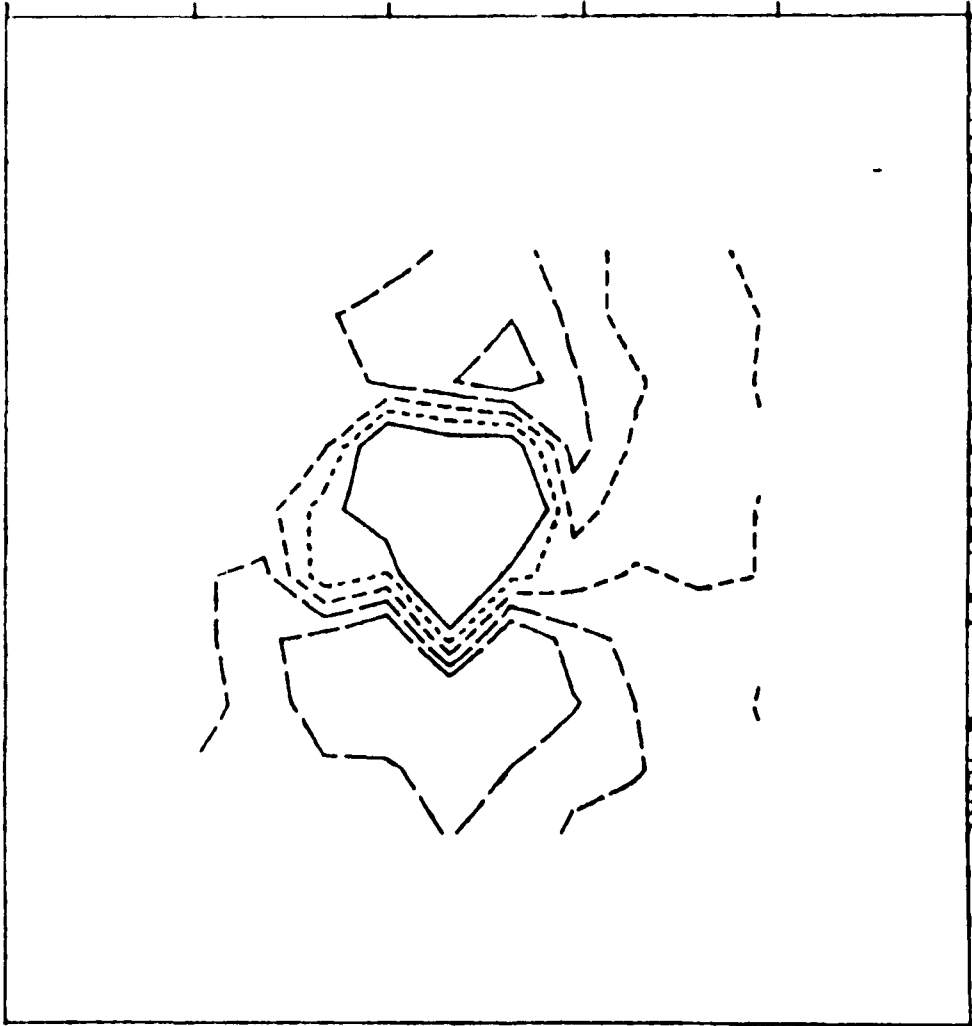
Figure A-1

3 INCH PLANE

CTOTAL

10.500

-0.2000  
-0.1000  
0.0000  
0.1000  
0.2000



0.500 MIN Z = -0.5788 @ ( 2.859; 8.881 )

7.000

4.000

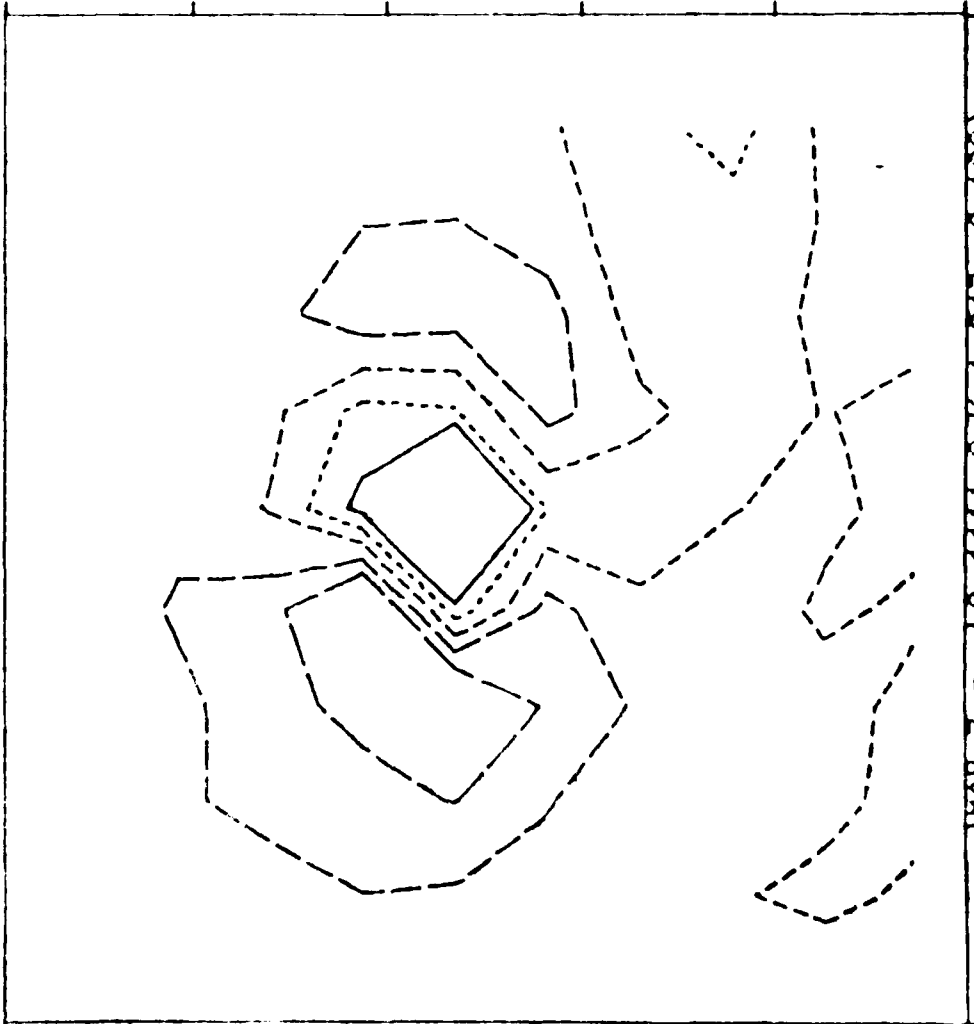
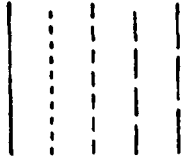
Figure A-2

4 INCH PLANE

CTOTAL

10.500

-0.2000  
-0.1000  
0.0000  
0.1000  
0.2000



7.000

4.000

0.500 MIN Z = -8:8365 @ ( 2:277, 8:657)

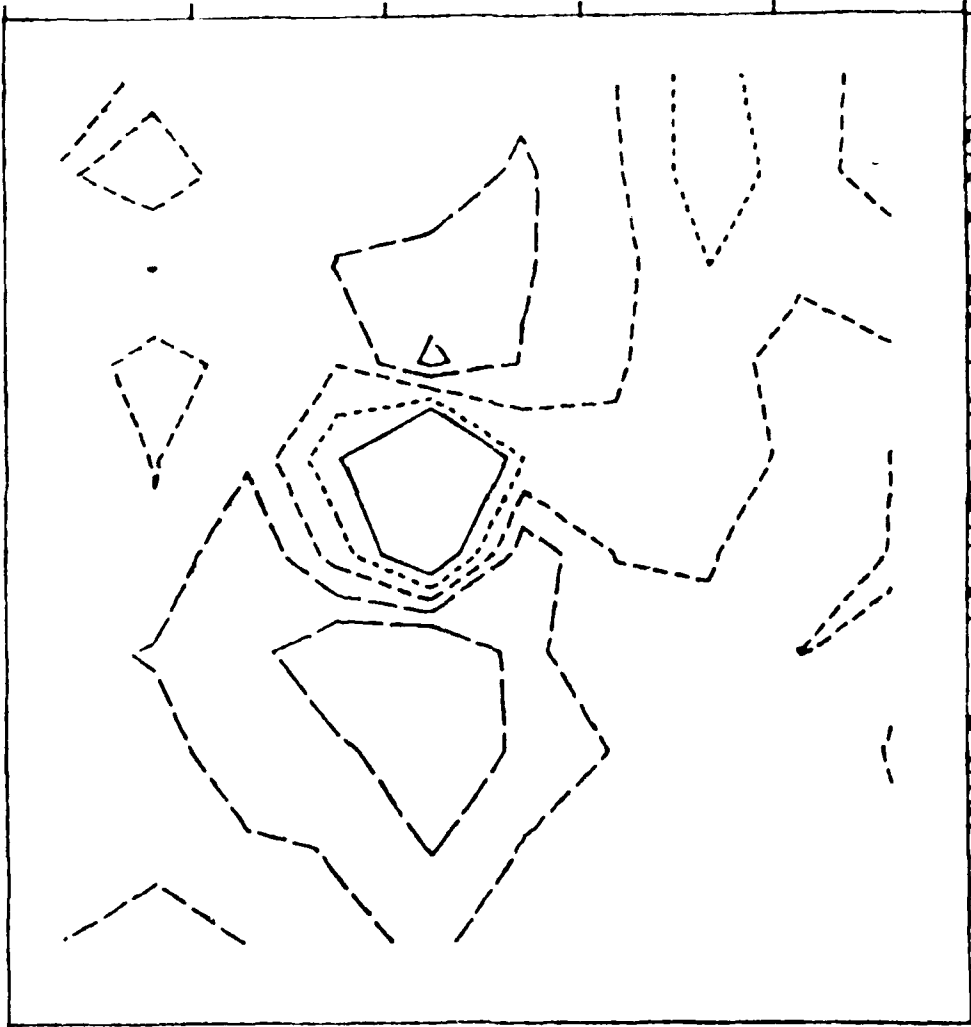
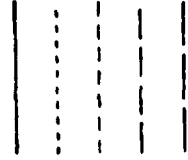
Figure A-3

6 INCH PLANE

CTOTAL

10.500

-0.2000  
-0.1000  
0.0000  
0.1000  
0.2000



7.000

4.000

0.500 MIN Z = -8:3189 @ ( 2:299; 8:947 )

Figure A-4

1 INCH PLANE

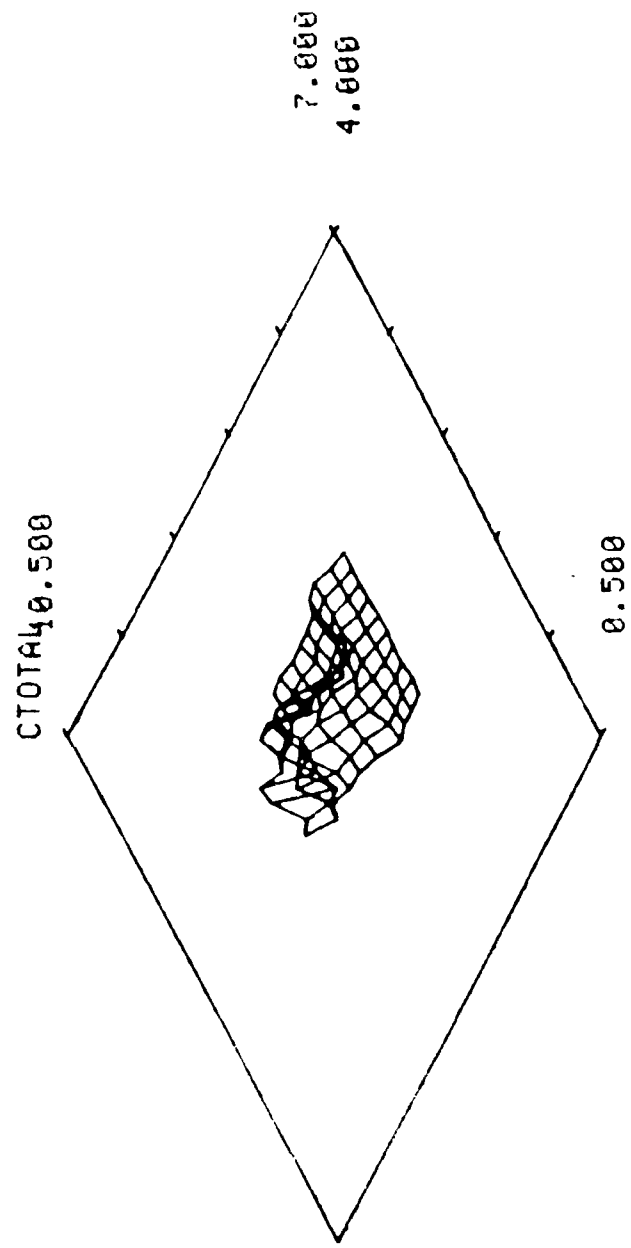
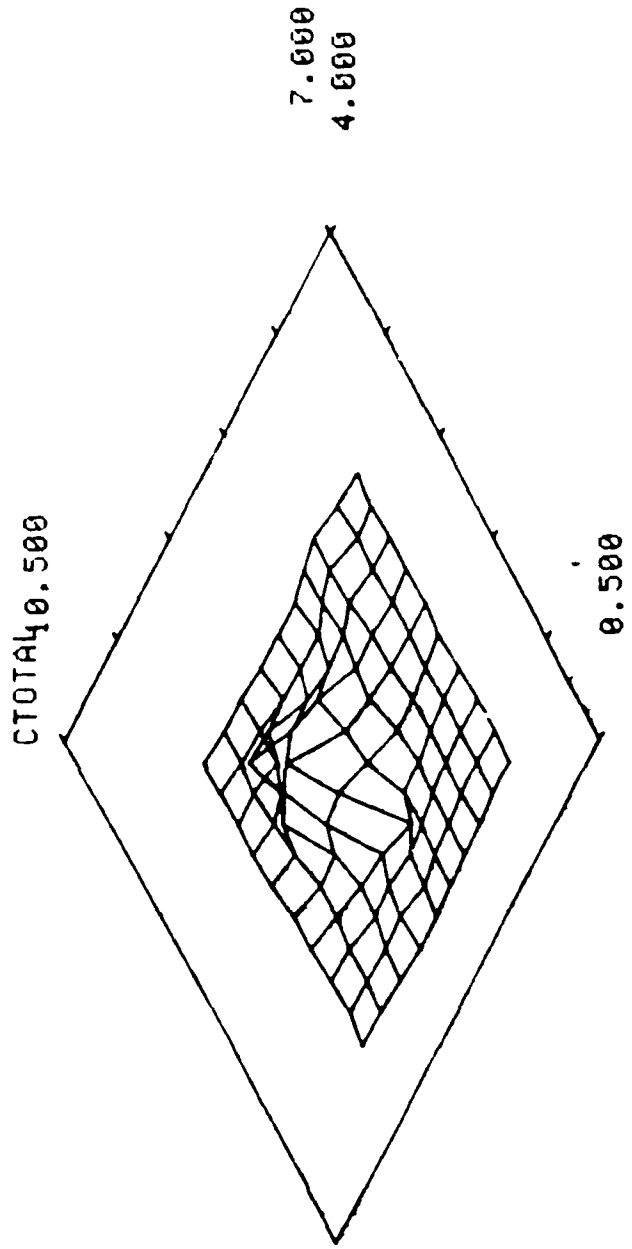


Figure A -5

2 INCH PLANE



A-6

Figure A-6

3 INCH PLANE

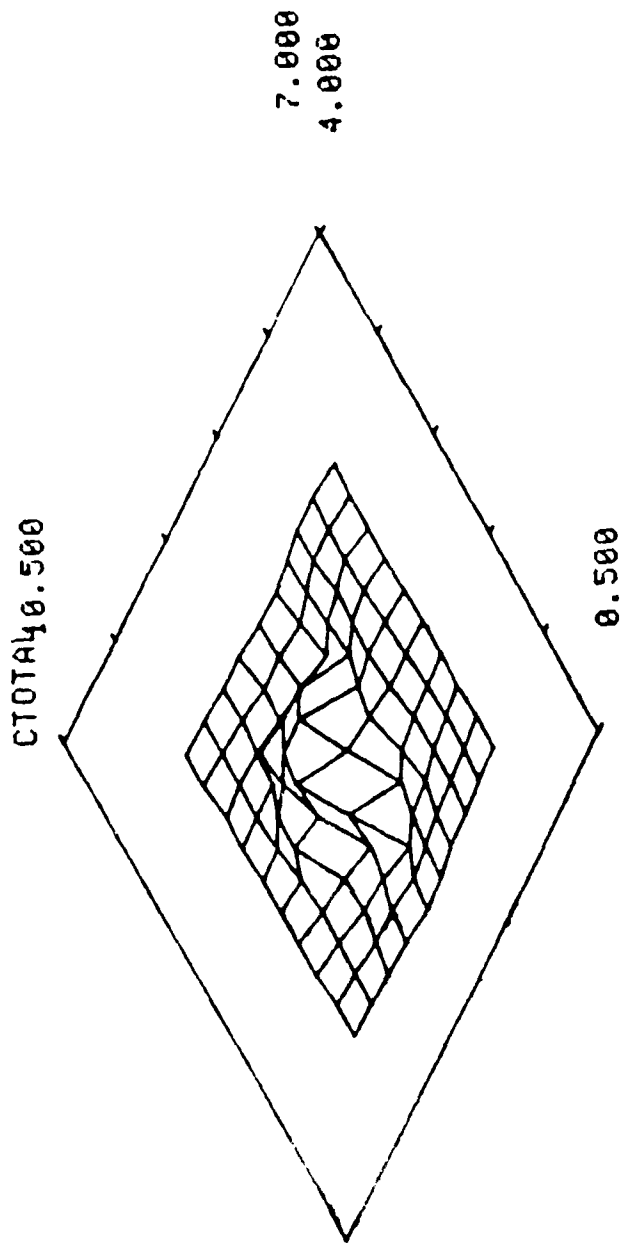


Figure A-7

4 INCH PLANE

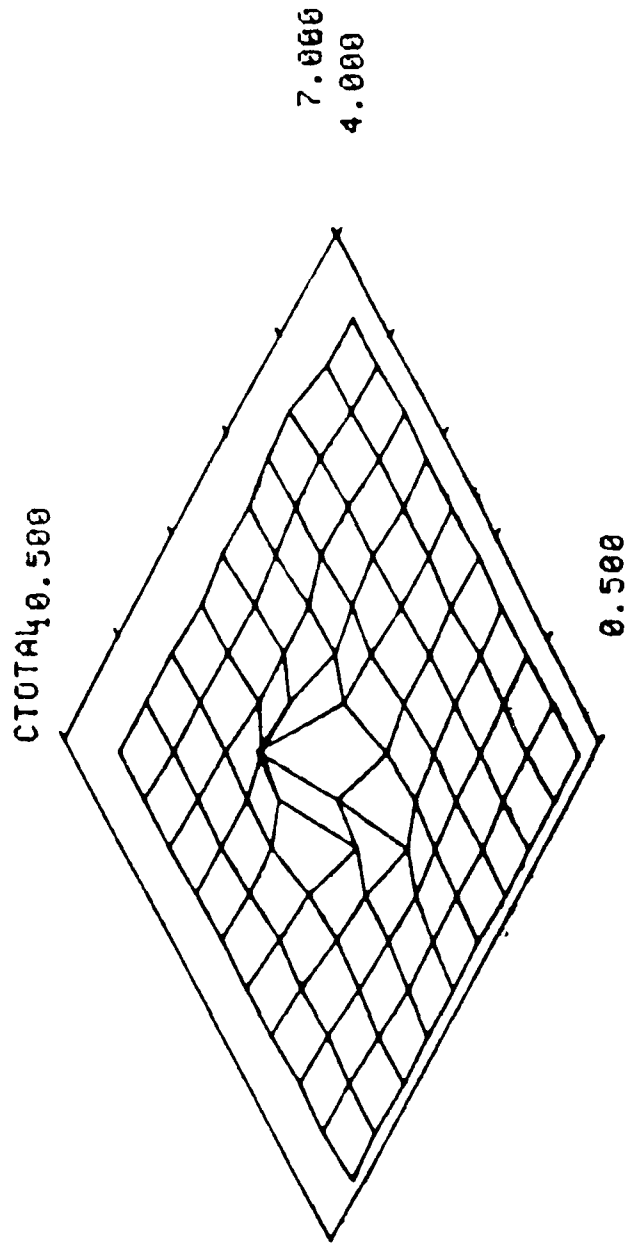


Figure A-8

**END**

**FILMED**

3-85

**DTIC**